PCCP

Exploring the kinetics of actinyl-EDTA reduction by ferrous iron using quantum-mechanical calculations

Journal:	*Physical Chemistry Chemical Physics*
Manuscript ID	CP-ART-10-2020-005179.R2
Article Type:	Paper
Date Submitted by the Author:	08-Feb-2021
Complete List of Authors:	Kim, Sooyeon; University of Michigan College of Literature Science and the Arts, Earth and environmental sciences Bender, Will; Geosyntec Consultants Inc; University of Michigan College of Literature Science and the Arts, Earth and Environmental Sciences Becker, Udo ; University of Michigan, Dept. of Earth and Environmental Sciences

PCCP

PAPER

Exploring the kinetics of actinyl-EDTA reduction by ferrous iron using quantum-mechanical calculations

Received 00th January 20xx,
Accepted 00th January 20xx

DOI: 10.1039/x0xx00000x

Sooyeon Kim,[a] Will M. Bender[ab] and Udo Becker*[a]

The reduction of An(VI) (An = U, Np, and Pu) to An(IV) significantly decreases its solubility and mobility. This reaction can be hindered by complexation with inorganic (*e.g.*, carbonate) or organic ligands. Ethylenediaminetetraacetic acid (EDTA) is one such organic ligand that forms stable complexes with actinides. Therefore, it may enhance the mobility of actinides. However, the redox kinetics and mechanisms of actinyl(An(V/VI)$O_2^{+/2+}$)-EDTA are not well characterized yet and are thus studied here using quantum-mechanical calculations. The principle is to approach the actinyl-EDTA and Fe^{2+} (reductant) in small incremental steps and calculate the system energy at each distance. The overall reaction is then delineated into sub-processes (encounter frequency in bulk solution, formation of outer-sphere complex, transition from outer- to inner-sphere complex, and electron transfer), and reaction rates are determined for each sub-process. The formation of outer-sphere complexes occurs rapidly in microseconds to seconds over a wide range of actinyl concentrations (pM to µM); in contrast, the transition to the inner-sphere complex is relatively slow (milliseconds to a few seconds). Immediate electron transfer to form the pentavalent actinide is observed along the reaction path for Np(VI) and Pu(VI), but not for U(VI). Surprisingly, in acidic conditions, one of the carboxylic groups gets protonated in EDTA of $[UO_2(edta)]^{2-}$ rather than one of the amino groups. This process-based series of calculations can be applied to any redox reaction and allows predicting changes to the rate law and rate-limiting step in a more fundamental way for different environments.

1. Introduction

The release of uranium contaminants from mining, processing of uranium ore, or waste disposal from nuclear power plants is of concern for human health and the environment.[1, 2] How the released uranium compounds transport in nature depends strongly on their oxidation states;[3] U(VI) is several orders of magnitude more soluble than U(IV). Thus, the transport of uranium contaminants is broadly hindered by the reduction to U(IV). Other actinides (An) such as Pu and Np also have low solubility under reducing conditions.

The reduction of actinyls ($AnO_2^{+/2+}$) is typically hindered by complexation with inorganic ligands, such as carbonate,[4-6] or organic ligands, such as citrate (Cit) or oxalate.[7-9] The behavior of actinyl carbonate complexes has been investigated broadly by experiments[5, 10] and computational methods[4, 6, 11] due to the stability and abundance of these complexes in nature. Thus, it is well known that the complexation with carbonate inhibits the reduction of actinyls. Morris[5] found the electron transfer rate of aquo-complexed uranyl to be two orders of magnitude faster than that of the tricarbonate complexed uranyl. Bender *et al*.[4] calculated the reduction rate of tricarbonated actinyls and found that electron transfer is unlikely to occur without coupled proton transfer from either the reductant or nearby water molecules, and the same was observed by Wander *et al*.[6] Citrate is an example of the organic ligands that slow down the reduction of U(VI). Reduction rates are slow, particularly at higher pHs where uranyl forms polymeric complexes with citrate, such as $[(UO_2)_6Cit_6(OH)_{10}]^{16-}$.[9]

Ethylenediaminetetraacetic acid (EDTA) is another example of organic ligands known to form stable complexes with metal ions. EDTA is widely used as a decontamination agent in the nuclear industry and agriculture. In the decontamination process, EDTA is used to dissolve contaminant films that may cover facility surfaces by forming strong complexes with a range of metal ions.[12] However, due to its low biodegradability, concentrations can build up quickly in groundwater and soil if released.[13, 14] Thus, there is a concern that the released actinides complexed with EDTA may be more mobile so that they could be transported further away from the original source. Wang *et al*.[15] found that EDTA-complexed U(VI) has a slower reduction rate than uranyl-hydroxide in experiments using bioreduced anthraquinone-2,6-disulfonate. The reduction rate trend in their experiments follows the ligand size; the smaller the complexed ligand size is, the faster the reaction is. It follows then that larger ligands may inhibit electron transfer, and EDTA is relatively large compared to hydroxides or carbonates.

However, in nature, microbes can facilitate the reduction of U(VI) in EDTA solutions by promoting electron transfer in the course of microbial metabolism.[16-18] In this situation, EDTA may serve as an electron donor or "food" for the microbial reduction

[a] Department of Earth and Environmental Sciences, University of Michigan, Room 2534, North University Building, 1100 N University Ave, Ann Arbor, MI 48109-1005, USA. Email: ubecker@umich.edu
[b] Geosyntec Consultants, 1111 Broadway, 6th Floor, Oakland, CA, 94607, USA.
†Electronic Supplementary Information (ESI) available: See DOI: 10.1039/x0xx00000x

mechanism. In some cases, EDTA itself may also function directly as an electron donor to reduce U(VI). Light sources, especially in the UV range, can reduce uranyl-EDTA through photocatalytic reduction. Several previous studies[19-21] have found that EDTA acts as an electron donor to reduce uranyl. Among all these potential mechanisms of uranyl-EDTA reduction, we only focus on the effect of EDTA complexation itself in this study.

While hexavalent uranyl is common under ambient conditions, Np(V) and Pu(IV) are the dominant species in aqueous solutions, but additional aspects need to be considered in the presence of complexing agents, *e.g.*, EDTA, such as complexation constants and reduction kinetics. In Reed *et al*.,[22] a rapid reduction from hexavalent to pentavalent species was observed in the presence of EDTA. Further reduction to the tetravalent state was observed for Pu, but not for Np in their experiments. Many previous studies have reported that Pu(IV) is the dominant oxidation state in the very strong Pu-EDTA complexes.[23-25] In terms of the kinetics, the reaction hurdle in these actinyl-EDTA reduction reactions has not yet been found. Thus, a molecular-level study explaining what inhibits or promotes the reduction of actinyls in the presence of the EDTA ligand is crucial.

Previous computational studies by Bender *et al*.[4, 26], Zarzycki *et al*.[27], and Taylor *et al*.[28] have calculated redox kinetics by dividing reactions into sub-processes. The sub-processes are the encounter frequency in bulk solution (*i.e.*, how often two species get close enough, typically < 8-10 Å), the formation of an outer-sphere complex (OSC), the transition from outer- to inner-sphere complex (ISC), and the transfer of electrons. In this context, an OSC is defined as a configuration where the hydration spheres of the reductant and oxidant are weakly bonded, typically by Coulomb attraction, while remaining intact. An ISC may then be formed when water molecules between the reactants are expelled from their respective hydration shells, such that the two species can be bridged by sharing one or more O^{2-}, OH^{-}, or water molecules and contained in one larger hydration shell. By breaking down the whole process into these four discrete steps, we can calculate the kinetics of each step and determine the rate-limiting one under specific environmental conditions. For example, Renock *et al*.[29] found through a similar computational approach that the oxidation of realgar (AsS) changes from oxidant dissociation being the rate-limiting factor to the actual electron/spin transfer at a given pH, thereby explaining the different rate laws at different pH and experiments.

In this study, we investigate the reduction kinetics of actinyl species (U, Np, and Pu) complexed with EDTA. This work aims to calculate the rate constants and reaction rates for the reduction of actinyl-EDTA complexes using quantum-mechanical calculations. From the system energy curves obtained as a function of the distance between the reactants, we can determine the energy barriers for each reaction sub-processes and ultimately can calculate reaction rates of those sub-processes. This helps identifying which of the four sub-processes (encounter frequency in bulk solution, the formation of outer-sphere complex, the transition from outer- to inner-sphere complex, and transfer of electrons) is the rate-limiting step of the actinyl-EDTA reduction. And by comparison with rate-determining experiments, we can also test if this approach captures the nature of the reaction mechanism correctly.

2. Methods

2.1. Quantum mechanical calculations

Geometry optimizations of the molecular systems, followed by electronic structure and vibrational frequency analyses, were calculated using the density functional theory (DFT)-based Gaussian09 software package. Calculations were performed using the B3LYP hybrid functional,[30, 31] which has produced reliable results in terms of thermodynamic properties and geometries for actinide complexes[32-35] and for ferrous iron.[36] For example, the calculations of reduction free energies of actinide complexes by Arumugam and Burton[34] resulted in a good agreement with experimental values using B3LYP. Therefore, we chose B3LYP in this study but performed a test using other density functionals (PBE0[37] and M06L[38]) in order to quantify the influence of different density functionals on the reaction energy barriers. The results of this comparison and associated discussion can be found in Table S1 of the Supplementary Information.

The choice of basis set is also crucial but can also significantly increase the computational expense if a more rigorous one is applied. Thus, we performed a test to see the effect of different basis sets on the reaction kinetics of our system (Table S2). The Stuttgart relativistic small-core basis set with its corresponding pseudopotential sets[39, 40] was compared to the Stuttgart relativistic large-core basis set and its pseudopotentials.[41]

Among the tested basis sets, a combination of LANL2DZ (for H, C, O, and N)[42, 43] and Stuttgart relativistic small-core basis sets (for Fe, U, Np, and Pu)[39, 40] with their corresponding pseudopotential sets (that include 10 core electrons for Fe and 60 for the actinides) were used in this study. Calculations using small-core ECP in combination with B3LYP by Schreckenbach and Shamov[44] produced very good reaction energies and optimized geometries of uranyl complexes compared to the values obtained from the experiments. The same combination was used by Bernardo et al.[35] and Batista et al.[45] for the calculation of reaction energies and vibrational frequencies of U(VI) complexes, which showed good agreement with experimental data.

In order to calculate the kinetics of reactions between the actinyl-EDTA complex and a reductant (Fe^{2+}), several series of geometry optimization calculations were performed to obtain a system energy curve as a function of the distance between actinide and Fe^{2+}. For all series of calculations, reaction pairs (actinyl-EDTA and Fe^{2+}) were put at an initial distance of 10-12 Å. At this far a distance, the actinyl-EDTA complex and the reductant are separated sufficiently, such that there is little interaction between them in an aqueous solution. During the series of calculations, the reductant ion with its hydration shells was moved by 0.25 Å towards the actinide at each step until they were closer than the optimized ISC distance (< 4 Å). At every step, the distance between actinide and reductant was

kept constant with the origin of the system set to be the An (An = U, Np, and Pu) atom, and geometry optimization was performed on all other atoms in EDTA, reductant, and the hydration spheres. The starting electronic configuration for each step was taken from the wavefunction of the previous step geometry.

It is well known that ferrous iron has octahedral coordination in aqueous water[46, 47]. However, when it bonds with ligands, such as hydroxides, it can change its ground state geometry or spin multiplicity. Two hydroxides were added in order to balance the charge of Fe^{2+} to minimize electrostatic attraction between the negatively charged actinyl-EDTA complex and the charge of the Fe^{2+} complex. In an actual aqueous system with a complex and varying composition of cations and anions, charge neutralization would take place in the first or second coordination sphere in a similar way, but testing the plethora of possible combinations of complexations is beyond the scope of this study. Four explicit water molecules in addition to the two hydroxides were used for the first hydration shell. Eight more water molecules for the second shell were inserted to represent a more realistic model ($Fe(OH)_2(H_2O)_{12}$) to study the influence of breaking through the hydration shells on the overall reaction kinetics. Typically, there are twelve or thirteen water molecules in the second hydration shell with a range of bond strengths (this result, however, depends to a certain degree on the timescale of observation and, therefore, on the method).[48-50] However, we only added the necessary number (eight) of explicit second-shell water molecules located at the next-nearest distance outside the first hydration shell of Fe. These are also the most strongly bond water molecules of the second hydration shell. Of those, the water molecules between the two complexes are the most important for determining the kinetics. Pre-optimization of the reductant unit moved one of the hydroxides to the second hydration shell leaving only one hydroxide in the first shell. The resulting $Fe(OH)(H_2O)_5^+$ complex prefers octahedral coordination with a high-spin state.[51] Our optimized geometry with a high-spin state agrees well with the experimental data for Fe-OH_2 distance (~2.15 Å)[52, 53]. A slightly longer distance of Fe-OH (2.0 Å) was obtained compared to the literature data (1.83 Å)[51], likely due to the addition of the second hydration shell.

Five explicit water molecules were used for the hydration shell of actinyl-EDTA to complete coordination in the equatorial plane of the actinyl-EDTA complex. Three of them were placed in the equatorial plane of the actinide, making the coordination number of An in this plane as five, and the remaining two more water molecules were placed away from the equatorial plane but bonded to the three water molecules in the equatorial plane of the An. The Conductor-like Polarizable Continuum Model (CPCM)[54] was employed to simulate an aqueous environment around the explicit water molecules as a dielectric fluid. The configuration of uranyl-EDTA with explicit water molecules is described in more detail in Section 3.1.

Depending on the charge of actinyl (+5 or +6), the total system charge was set to be -2 or -3. Both ferromagnetic (FM, same spin direction on the Fe and An) and anti-ferromagnetic (AFM, opposite spin directions) electron configurations were calculated for actinides and Fe^{2+}. However, since electron transfer was only observed for the AFM electron configuration, all the results shown here use the AFM electron configuration. In addition, with an AFM configuration, the system maintains its overall spin and, therefore, angular momentum during electron transfer going from U(VI, $0\uparrow$) + Fe(II, $4\downarrow$) to U(V, $1\uparrow$) + Fe(III, $5\downarrow$). This is spin allowed and thus, a kinetically and thermodynamically more favorable reaction. Charge and spin were analyzed using Bader population analysis on the optimized geometry at each step and are described in Section 3.5.

2.2. Calculation of reaction rates

Energy curves as a function of An-Fe^{2+} distance were obtained from several series of DFT calculations. The general concept is that each curve starts with a flat plateau at a far distance (approximately 10-12 Å) and transitions to a shallow slope as the two reactants begin "feeling" each other by Coulomb interactions or long-range polarization effects. At least two energy minima along the curve are expected associated with outer- and inner-sphere complexes. The energy barrier between these two energy minima is the activation energy to force the reaction from the outer-sphere complex to the inner-sphere complex; this activation energy can be conceptualized by the effort to "squeeze" the water out between oxidant and reductant. Additional energy minima can arise from a barrier for electron transfer and/or from the formation and breaking of hydration bonds.

Reactant encounter and outer-sphere complex formation. To calculate the reaction rates of each sub-process mentioned above, we describe here how to determine the reaction rates of those sub-processes. In order to form an outer-sphere complex, reactants must first encounter in the bulk solution. When the two reactants meet each other and gain energy greater than one k_BT unit (2.48 kJ/mol at 298.15 K) compared to the system energy with the infinite separation distance between the two reactants, the slope of the energy curve becomes steeper so that the two species are close enough to proceed further attraction toward the formation of outer-sphere complex. While the back reaction into the solution is built into the calculation system, typically, the activation energy from the outer-sphere complex to the solution is so high that little of this back-reaction actually occurs.

The distance where the system has an energy gain of one k_BT unit is defined as the reactive radius (R_r), which is used to calculate the reaction rate of encounter complex formation. Based on collision theory,[55] the encounter complex formation rate can be calculated using eqn (1).

$$r = \pi R_r^2 \nu N_A [X][Y] \quad (1)$$

where R_r is the reactive radius, v is the geometric mean of the diffusion velocities of the reactants, N_A is the Avogadro's number, and [X] and [Y] are the concentrations of the reactant species. Diffusion coefficients to calculate diffusion velocities were taken from the literature: 7.19×10^{-10} m^2/s for Fe^{2+}, 3.22×10^{-10} m^2/s for uranyl-EDTA, 1.4×10^{-10} m^2/s for neptunyl-EDTA, and 3.54×10^{-10} m^2/s for plutonyl-EDTA.[56-60] We assume

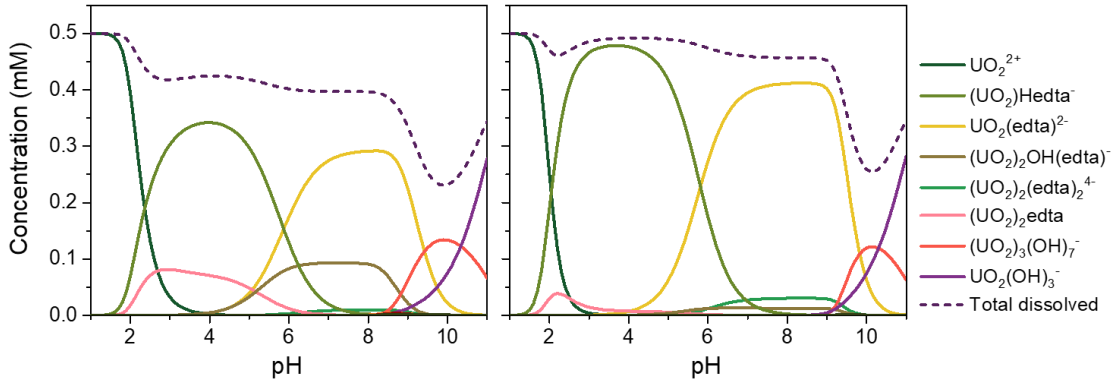

Fig. 1 UO_2-EDTA speciation as a function of pH. (a) $[UO_2^{2+}]$=0.5 mM and [EDTA]=0.5 mM, (b) $[UO_2^{2+}]$=0.5 mM and [EDTA]=2 mM

that different actinyl charge states have no effect on the diffusion coefficient because the differences have been shown to be minor.[4, 61] In systems with [Y] being in great excess of [X] (it is likely in natural systems that the iron concentration is much higher than the actinyl one), eqn (1) can be simplified to a pseudo-first-order rate which depends on the concentration of species X (An-EDTA complex). Since the concentrations of the actinyl complexes are typically very low (pM to μM range) in environmental settings, our model can be considered a pseudo-first-order reaction.

Inner-sphere complex formation and electron transfer. After the formation of an outer-sphere complex, the two reactants can proceed to form an inner-sphere complex. As the reactants approach each other, other outer-sphere complexes can be temporarily formed, assuming different geometries of the first coordination and hydration shells (evident as the additional local minima in the energy curve), or the inner-sphere complex can be formed directly. During the formation of an inner-sphere complex, some of the first-coordinated water (or OH^-) have to be squeezed out of the gap between the reactants, which then share bridging H_2O, OH^-, or O^{2-} molecules between them and form a larger hydration shell containing both reactants. In this process, energy input is required to push out the water molecules between the reactants, which appears as an energy barrier between the outer- and inner-sphere complex. The reaction rates of transition from outer- to inner-sphere complex depend on this energy barrier, as described by the Arrhenius equation.

$$k_r = Ae^{-\frac{E_a}{RT}} \quad (2)$$

where k_r is the rate constant (s^{-1}), A is attempt frequency (s^{-1}), E_a is activation energy (J mol^{-1}), R is gas constant (J mol^{-1} K^{-1}), and T is the temperature (298.15 K). Attempt frequencies (A) also depend on activation energies and can be calculated according to eqn (3).[62-64]

$$A = \frac{1}{\sqrt{2}}\sqrt{\frac{E_a}{m\lambda^2}} \quad (3)$$

where m is the mass of the moving unit (the reductant including its hydration shells in this study), and λ (m) is the distance between the two energy minima separated by the activation energy barrier. This equation was originally applied for the diffusion of atoms in bulk or on the surface of the periodic crystal. An alternative way to calculate the attempt frequency is to use the curvature of the energy curve near an energy minimum; however, this second method tends to rely too much on the very local electronic structure about the minimum, and therefore, eqn (3) is more convenient in a lot of cases discussed here. In addition, Bender *et al*. verified that attempt frequencies calculated using eqn (3) are very similar to the ones calculated by the parabolic curve fitting.[26] Electron transfer can occur at any sub-processes during the redox reaction, typically occurs at the outer- or inner-sphere complex stage. A full description of the electron transfer rate would be available using Marcus theory. However, we will explore it using only the system energy curve by analyzing the change of charge and spin density of actinides and Fe along the reaction paths, because of the high computational cost required for Marcus theory calculations.

In order to study the overall reaction kinetics encompassing all sub-processes, concentration changes of each species over time was calculated using a computer code developed at Bender *et al*.[26] Both forward and backward reactions of inner-sphere complex formation were considered along with the formation rate of outer-sphere complexes from the bulk solution calculated using eqns (1) – (3). Further information about the method used here is described in detail in our previous study.[26]

3. Results

3.1. Actinyl-EDTA speciation

In order to better understand the actual species that may be responsible for controlling the kinetics of complexation and potentially specific redox reactions, we start this section by evaluating the speciation of protonation and complexation. The type of actinyl-EDTA complexation varies as a function of pH. This is because EDTA has six pK_a values (0, 1.5, 1.99, 2.67, 6.16, 10.26), the lower four from the protonation of the carboxyl functional groups and the two higher ones from the amino groups.[65-67]

$$H_6(edta)^{2+} \leftrightarrow H_5(edta)^+ + H^+ \qquad pK_{a1} = 0 \quad (4)$$

$$H_5(edta)^+ \leftrightarrow H_4(edta) + H^+ \qquad pK_{a2} = 1.5 \quad (5)$$

$$H_4(edta) \leftrightarrow H_3(edta)^- + H^+ \qquad pK_{a3} = 1.99 \qquad (6)$$

$$H_3(edta)^- \leftrightarrow H_2(edta)^{2-} + H^+ \qquad pK_{a4} = 2.67 \qquad (7)$$

$$H_2(edta)^{2-} \leftrightarrow H(edta)^{3-} + H^+ \qquad pK_{a5} = 6.16 \qquad (8)$$

$$H(edta)^{3-} \leftrightarrow edta^{4-} + H^+ \qquad pK_{a6} = 10.26 \qquad (9)$$

Thus, the dominant species of EDTA (capitalization of EDTA is used here to refer to all different protonated forms of EDTA in an aqueous solution, and lower-case edta represents specifically $edta^{4-}$) in very basic solutions is $edta^{4-}$, and at a circumneutral pH, it would be $Hedta^{3-}$ (by convention in the literature, HEDTA would represent N-(2-hydroxyethyl)-ethylenediaminetriacetic acid, which has one hydroxyl group instead of a carboxyl group, therefore, Hedta is used in this paper to refer to $H(edta)^{3-}$). Accordingly, the dominant species of actinyl-EDTA complex varies with pH. Thus, determination of which species would be dominant at the pH ranges of interest is crucial when deciding which reactant to evaluate in our kinetics calculations.

The speciation of uranyl-EDTA complexes over a wide pH range was calculated using MINTEQ 3.1 (Fig. 1). For uranyl, the most dominant form at low pH (3 to 5) is $U(VI)O_2(Hedta)^-$, and $U(VI)O_2(edta)^{2-}$ becomes dominant at pH values > 6. As the U/EDTA ratio decreases, the concentration of total dissolved aqueous uranyl increases, with the same dominant species at different pH ranges; Fig. 1(b) shows a higher total dissolved aqueous uranyl species concentration (dotted line) than Fig. 1(a).

Since $UO_2(edta)^{2-}$ is the most dominant complex in the pH range from 6 to 10, we used this species to calculate the reaction kinetics using quantum-mechanical calculations at circumneutral pH, which is an environmentally relevant pH range. In addition, low pH ranges (~2.5-6) were modeled using $UO_2(Hedta)^-$ mimicking the pH conditions in environments such as acid mine drainage. The geometry of $UO_2(edta)^{2-}$ is not yet well characterized, but previous studies[65, 68-70] suggest some. Due to the linear configuration of actinyl, there are steric limitations for the structures of actinyl complexes. Thus, mainly the equatorial plane is involved in the complexation with ligands. Based on the EXAFS (Extended X-ray Absorption Fine Structure) studies using HEDTA, which has a similar structure with EDTA, Li *et al*.[69] proposed a tridentate geometry of EDTA coordinated by two carboxylates and one N, leaving the other two carboxylates and N not coordinated to the neptunyl center. Brighli *et al*.[68] proposed a tetradentate geometry by two carboxylates and two N such that EDTA wraps the uranyl center in the equatorial plane.

In this study, the geometry proposed by Brighli *et al*.[68] was used as a starting point for the calculations. The reason for using this geometry is that it resulted in the lowest system energy for the $UO_2(edta)^{2-}$ complex in our DFT calculations. Since it has been reported that uranyl in solution is coordinated to five water molecules in its equatorial plane,[71, 72] two water molecules were included in the equatorial plane of uranyl to make the coordination number of uranyl at least five when testing the geometry of complexation. Geometry optimizations using the two different geometries resulted in 62.5 kJ/mol lower system energy for the tetradentate geometry than the tridentate one. In this tetradentate geometry, the two carboxylates of EDTA are coordinating in the equatorial plane of UO_2^{2+}, and the other two carboxylates are free to rotate around the C-N bond. For the production run, we added three explicit water molecules around the equatorial plane of uranyl, such that the uranyl has total coordination of five in its equatorial plane (Fig. 2a). These three water molecules are the most tightly bound ones in the hydration sphere of the complex, and more loosely bound water molecules in the hydration sphere are modeled using two extra water molecules and the dielectric fluid (CPCM). Thus, the three water molecules in the equatorial plane are the rate-controlling ones for the kinetics step of dehydration, and therefore, they are needed to calculate the formation of outer- and inner-sphere complexes with the reductant species. The same geometry was used for the reduction of Np and Pu complexes (Fig. S1).

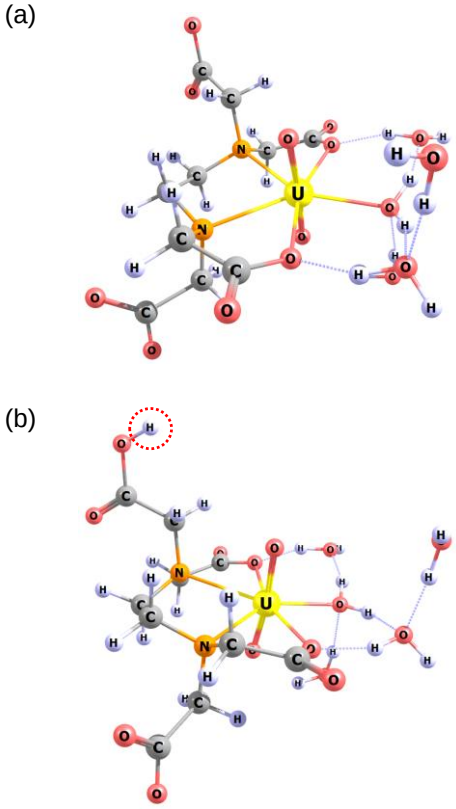

Fig. 2 Suggested configuration of (a) $UO_2(edta)^{2-}$ and (b) $UO_2(Hedta)^-$ (with protonation visible in the red dotted circle), with three water molecules on the equatorial plane of UO_2^{2+}. White-H, gray-C, red-O, orange-N, and yellow-U. The dotted gray lines indicate hydrogen bonds.

In acidic conditions, as the solution pH decreases, the species begin to be protonated. The first protonation site of $edta^{4-}$ is one of the two N of EDTA according to the pK_a values of EDTA (pK_a of 6.16 and 10.26). However, when the uranyl is complexed with EDTA, Brighli *et al*.[68] proposed that the first protonation site is one of the free carboxylates, based on the protonation constants of $UO_2(edta)^{2-}$. Test runs in this study using a $UO_2(Hedta)^-$ geometry optimization with protonation on one of the N resulted in the transfer of a proton from N to a nearby

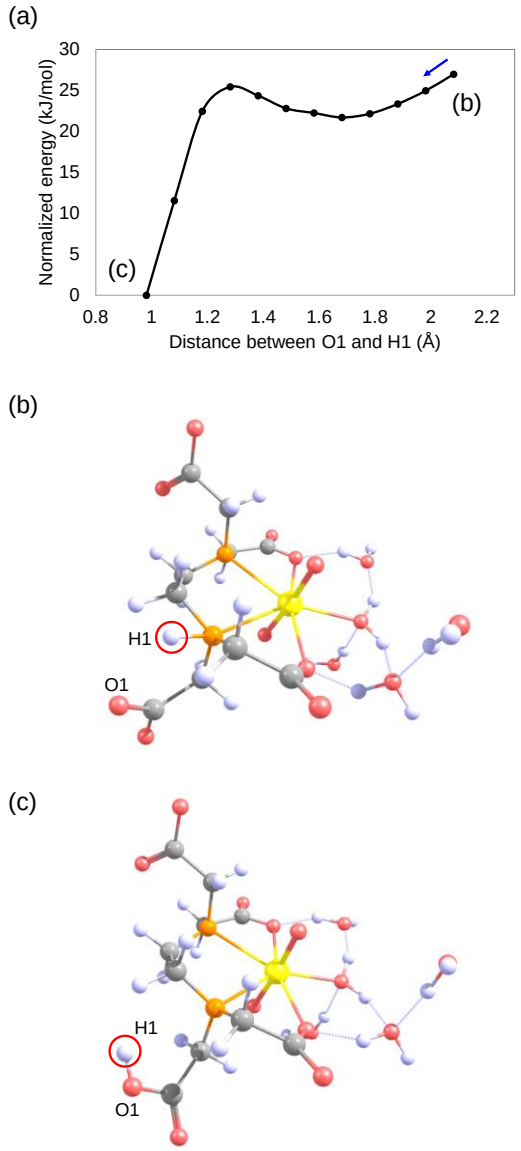

Fig. 3 (a) System energy scan along a proton transfer path from N to the nearby carboxylate O. The starting geometry of $UO_2(Hedta)^-$ is (b) a proton (H1) on one of the N, and then the proton moves over to O1 by 0.01 Å every step. The final geometry is (c) H1 bonded to O1. White-H, gray-C, red-O, orange-N, and yellow-U. The dotted gray lines indicate hydrogen bonds.

carboxylate (and not to nearby water molecules). The reason for this is that N is already coordinated to An (An = U, Np, or Pu) with a coordination number of five in the equatorial plane, and the strong An-N bond would be hard to break, which is necessary for the protonation of N. Fig. 2(b) shows the geometry of $UO_2(Hedta)^-$ suggested and used in this study. Moreover, the system energy becomes more stabilized by this proton transfer (Fig. 3).

An energy scan of the proton transfer process (Fig. 3a) was performed by moving a proton from N of EDTA to the nearby carboxylate. Everything except the distance between H1 and O1 was allowed to relax, and then the system energy was calculated by moving the proton in 0.1 Å steps. The stabilization energy due to the proton transfer is about 27 kJ/mol with an activation energy barrier of 3.7 kJ/mol. The energy barrier increases if the proton is transferred through the water chain nearby (when explicit water molecules are included in the model) through proton hopping, but it would most likely prefer the lowest energy path. Therefore, this proton transfer is not kinetically hindered, and it is thermodynamically favorable. The position of the proton in Fig. 3(b) is different from Fig. 2(b), but if there are water chains nearby, the proton can jump to the position shown in Fig. 2(b), which is an energetically even more favorable position.

3.2. Reaction energy curves

The energy curves as a function of distance for the six reactant pairs, the oxidants $[AnO_2(edta)]^{-2/-3}$ (An= U, Np, and Pu) and reductant $(Fe(OH)_2(H_2O)_{12})$, were calculated to derive kinetic parameters of the redox reactions of those pairs (Fig. 4). From those energy curves, we obtain reactive radii (R_r), activation energy barriers (E_a and $E_{a,back}$), and distances between the two energy minima (λ) (Table 1). The reaction rates and rate constants can then be calculated using these parameters. Details of the values derived here are discussed in the following sections.

All the curves shown in Fig. 4 have two deep energy wells corresponding to inner- and outer-sphere complexes, and there can be one or more local minima or energy wells for both the inner- or outer-sphere complexes. Some little bumps in the energy curves result from forming (curve down) or breaking (curve up) hydrogen bonds.

Table 1. Calculated parameters for the kinetics calculation from the reactions between $[AnO_2(edta)]^{2-/3-}$ and $Fe(OH)_2(H_2O)_{12}$ using the CPCM solvation model. Reactive radii (R_r), activation energy barriers (forward E_a and backward $E_{a,back}$), and distances between the two energy minima (λ) are listed. ISC 1 and ISC 2 for $NpO_2(edta)^{2-}$ are consecutive steps as shown in Figs. 4(c).

Actinyls	Reactive radius (Å)	Activation energies (kJ/mol)		λ (Å, distance between energy minima)
		E_a	$E_{a,back}$	
UO_2^{2+}	8.6	60.5	49.7	2.75
UO_2^{+}	7.9	56.1	70.0	1.75
NpO_2^{2+}	8.2	71.4	143.0	2.25 (ISC 1)
		33.1	34.7	0.75 (ISC 2, w/ ET)
NpO_2^{+}	9.5	50.5	63.7	2.5
PuO_2^{2+}	8.3	67.4	80	1.25
PuO_2^{+}	7.7	49.2	52.2	1.75

Those small energy bumps due to changes in hydration bonding are formed randomly depending on the surrounding water geometries, so we went forward and backward along the reaction path to increase the number of the modeled water geometries to average out those effects. In addition, we calculated the hydrogen bond contributions of the system to eliminate the fluctuation of the energy curve due to the hydrogen bond, especially at the An-Fe distance below 6 Å, where hydrogen bond formation and breaking plays the most significant role. Hydrogen bond contributions were

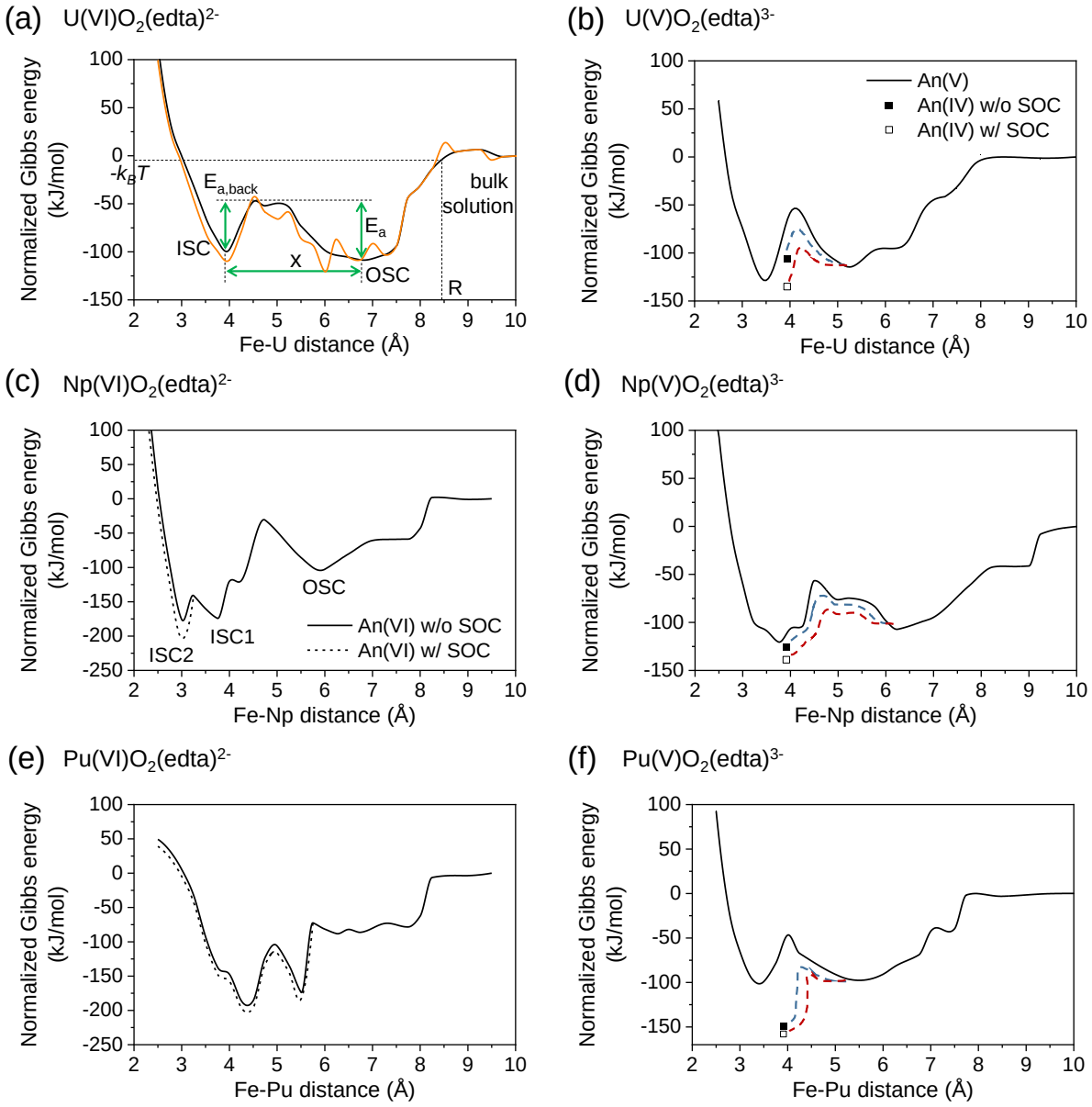

Fig. 4 Calculated energy curves for the actinyl-EDTA complexes with $Fe(OH)_2(H_2O)_{12}$ as a function of distance: (a) $UO_2(edta)^{2-}$, (b) $UO_2(edta)^{3-}$, (c) $NpO_2(edta)^{2-}$, (d) $NpO_2(edta)^{3-}$, (e) $PuO_2(edta)^{2-}$, and (f) $PuO_2(edta)^{3-}$ complex. The system energy is normalized such that the system is set to zero energy (i.e., $E(r=\infty)=0$) when the two reactants are separated and stay as independent aqueous species in bulk solution (An-Fe distances > 9.5 Å). The orange solid line in (a) is the normalized system energy obtained from the DFT calculations, and black solid lines are hydrogen bond corrected values. Only hydrogen bond corrected lines are shown for the rest of the species. The dotted lines are corrected energy including spin–orbit coupling (SOC). Only (c) and (e), which show the transition from hexavalent to pentavalent actinyls, are corrected by the SOC effect; details are discussed in Section 3.5. In (b), (d), and (f), closed square dots are tetravalent actinyls ISC energy without SOC effect, and open squares are with SOC effect. Estimated dashed lines are added, however without further information about the actual height of the activation barrier, for completion of the energy curve from OSC minimum of $An(V)O_2(edta)^{3-}$ to ISC minimum of An(IV)edta complex (blue - without SOC, red - with SOC).

approximated using variable $\varepsilon_{relative}$ that changes from 1 (no water between molecules) to 78.5 (in bulk), and then summed up the energy contribution of all hydrogen bonds. By comparing hydrogen bond contributions at each data point, original system energies were corrected for random changes in hydrogen bond energies in a particular reaction path. In Fig. 4(a), both the original curve (orange line) and the hydrogen bond corrected one (black line) are plotted to show how this hydrogen bond correction changes the original curve. For the rest of the curves, only hydrogen bond corrected curves are plotted. In an actual system, both complexes would find a reaction path that is not additionally aggravated by the breaking of hydrogen bonds, and thus, would follow more the "smoothed" curve shown, *e.g.*, in Fig. 4(a).

Proton transfer also occurs between the hydroxides and water molecules when the atoms rearrange as the reactants approach each other. This stabilizes the system energy and contributes to making local minima in the energy curves. For example, at one

of the local minima of the Np^{6+}-Fe^{2+} curve at a distance of 3.75 Å (Fig. 4c), three proton transfer events are observed as coordinating water molecules rearrange. As a result of this, the system energy at this distance drops from -120 kJ/mol to -174 kJ/mol. The change in Fe coordination number (starting at 6, but typically changing to 5 or 4) contributes significantly to the energy gain when the two reactants approach each other.

All energy curves show more stable inner-sphere complexes than outer-sphere ones except for $UO_2(edta)^{2-}$ (Fig. 4). ISC formation for $UO_2(edta)^{2-}$ with Fe^{2+} is thermodynamically not favorable. However, the energy difference between the inner- and outer-sphere uranyl-EDTA complexes is small (< 11 kJ/mol). When comparing hexavalent to pentavalent species, uranyl-EDTA reactions with Fe^{2+} as a reductant show similar normalized energy well depths for UO_2^+ and UO_2^{2+}. However, reaction curves for hexavalent Np and Pu have deep energy wells, but not for the pentavalent ones. This indicates NpO_2^{2+} and PuO_2^{2+} show significantly stabilized inner-sphere complexes. For these two cases, electron transfer occurs along the reaction path, so the actinides of the inner-sphere complexes were in reduced forms of each reactant (Np^{5+} and Pu^{5+}). For those actinyls to be reduced in the course of their reaction pathways, spin-orbit coupling (SOC) was considered and shown as dotted lines in Fig. 4 (c and e). For heavy elements with higher nuclear charges, spin-orbit interactions have a strong impact on chemical bonding and reactivity. The SOC for 5f orbitals of actinyls has been reported in previous studies.[73-75] Here, we used the values calculated by Vallet *et al*.[74]

For pentavalent actinides, no further reduction to tetravalent actinides was observed unless the geometry towards a tetrahedral bonding environment of the tetravalent actinide ion was manually and significantly rearranged. We calculated the energies for the optimized ISC geometries of An^{4+}-$edta^{2-}$ (An = U, Np, and Pu) with Fe^{3+} by rearranging the atoms manually, with and without SOC (square dots in Fig. 4(b, d, and f). An estimated line (dashed lines) is added in Figs. 4(b), (d), and (f) for the completion of the energy curve, by connecting the An(V)-EDTA OSC minima to their ISC with reduced actinyl forms, An^{4+}-$edta^{2-}$ with Fe^{3+}. The actual paths for these reductions involve not only rearrangements of the ligands around the An centers but also proton transfers through the solution; thus, these paths are too complex to be evaluated here. More details will be discussed in the following sections.

3.3. Outer-sphere complex formation from aqueous bulk-solution species due to collision

From the series of energy calculations with decreasing distance between reactants by small increments (< 0.25 Å), there is a distance at which the system energy is one k_BT unit (2.48 kJ/mol at 298.15 K) below the energy plateau where both reactants are completely separated in solution. This distance is defined as reactive radius (R_r) and is used to calculate the reaction rates of outer-sphere complex formation from the aqueous species in bulk solutions using eqn (1). Because the formation of hydrogen bonds between the water molecules around $[AnO_2\text{-EDTA}]^{2-/3-}$ and $Fe(OH)_2(H_2O)_{12}$ lowers the system energy, different explicit water geometries around the reactants result in different R_r values. In addition, these distances vary between the different actinyl species and their oxidation states, having a range of 7.7-9.5 Å (Table 1).

Both uranyl-EDTA and plutonyl-EDTA show shorter R_r for the reduced form. The water molecules and EDTA bound to actinide centers are more tightly bonded to hexavalent actinides (U^{6+}, Pu^{6+}) than pentavalent actinides (U^{5+}, Pu^{5+}). This tighter bonding probably makes the distance between the two reactant units longer and result in a longer R_r. The distance of U-O_{water} (O is from the nearest water in the equatorial plane) is 2.45 Å for UO_2^{2+} and 2.54 Å for UO_2^+ when the two reactants are completely separated. In the same manner, the distance between Pu and O_{water} is 2.43 Å for PuO_2^{2+} and 2.55 Å for PuO_2^+. Neptunyl-EDTA shows a different pattern with longer reactive radii for Np^{5+} than Np^{6+}. This is due to the orientation of the water shell around the reactants when they approach each other, which affects the formation of hydrogen bonds between the two reactants. $[NpO_2(edta)]^{3-}$ forms one hydrogen bond with the reductant unit at 9.0 Å and another one at 7.75 Å (Fig. 4d). In contrast, $[NpO_2(edta)]^{2-}$ forms two hydrogen bonds at 8.0 Å (Fig. 4c), which drops the system energy significantly. Consequently, the amount of system energy gains due to hydrogen bond formation for the two different oxidation states of Np are similar (~60 kJ/mol) at ~7.75 Å of Np-Fe distance. The distance between Np and O_{water} is 2.43 Å for NpO_2^{2+}, and 2.57 Å for NpO_2^+ when the two reactants are completely separated, which is the same trend with U and Pu.

When the reactants reach their reactive radii, they start to interact in an energetically favorable way. In the course of our series of calculations, as the actinyl-EDTA complex and reductant get closer, they start forming an outer-sphere complex. The reaction rate for the formation of the outer-sphere complex can be calculated using collision theory, as mentioned in the Methods section eqn (1).

Since aqueous Fe complexes are much more common in the environment than actinyls, we set reductant concentrations to be 1000 times higher than the concentration of actinyl-EDTA species in our calculations. With significantly higher concentrations of reductants, all actinyl-EDTA will react to form outer- or inner-sphere complexes eventually. Most of the aqueous actinyl-EDTA complexes were consumed very rapidly with 1 μM or 1 nM of actinyl-EDTA complex (in a few micro-seconds). However, with a very low concentration of actinyl-EDTA (1 pM), it would take a few seconds for all the aqueous species to be consumed because of the low probability of collision.

The half-life time ($t_{1/2}$) of aqueous actinyl-EDTA (*i.e.*, the time at which half the actinyl complex has already collided with the reductant species) is a good indicator for how fast those reactions occur. Since one of our reactants is more highly concentrated and thus does not get significantly consumed during the reaction, the reaction can be considered a pseudo-first-order reaction as mentioned in the Methods section, and $t_{1/2}$ can be calculated using eqn (10).

$$t_{1/2} = (ln\ 2) / (\pi R_r^2 \nu N_A[Y]) \quad (10)$$

where $t_{1/2}$ is in seconds, using Y as a species with a higher concentration. With a longer reactive radius, it takes less time to collide and react with the reductant, and the reaction rate is faster. Thus, $[UO_2(edta)]^{2-}$ has a shorter $t_{1/2}$ than $[UO_2(edta)]^{3-}$ due to its longer reactive radius (Table 2). With the same U:Fe ratio, $t_{1/2}$ decreases with the increase of reactant concentrations, as shown in Table 2, because, with higher concentration, there is a higher probability of collision. Increasing the U:Fe ratio also increases the initial collision rate for a given Fe concentration and leads to a faster reduction of the actinide. For example, with the same 1 mM Fe^{2+} concentration, 1µM of $[UO_2(edta)]^{2-}$ results in a 1000 times higher initial collision rate than 1 nM solution. However, $t_{1/2}$ does not change unless the Fe^{2+} concentration changes.

Table 2 Half-lives ($t_{1/2}$, time at which half of the actinyl complexes has collided with reductant) of aqueous actinyl−EDTA complexes in solutions with aqueous Fe^{2+} as a reductant. Reductant Fe^{2+} is 1000 times more concentrated in solutions than actinyl, for all different actinyl concentrations.

[actinyl-EDTA]	1 µM	1 nM	1 pM
[reductant Fe^{2+}]	1 mM	1 µM	1 nM
UO_2^{2+}	415 ns	415 µs	415 ms
UO_2^{+}	486 ns	486 µs	486 ms
NpO_2^{2+}	682 ns	682 µs	682 ms
NpO_2^{+}	515 ns	515 µs	515 ms
PuO_2^{2+}	424 ns	424 µs	424 ms
PuO_2^{+}	484 ns	484 µs	484 ms

3.4. The transition from outer- to inner-sphere complex

Energy curves show plateaus with little changes in geometry or electron configurations when the two reactants are separated by a distance of over ~10 Å. As they approach each other step by step, hydrogen bonds are formed between the water molecules in the hydration shells of actinyl-EDTA and the reductant. The energy gain from the formation of these hydrogen bonds makes the energy curve steeper with a downhill slope towards shorter separations, and the actinyl-EDTA complex starts to tilt toward the reductant. Thus, the $AnO_2^{+/2+}$ axis is not perpendicular anymore to the An-Fe connection. This tilting occurs because of the negatively charged oxygen of $AnO_2^{+/2+}$ being attracted by hydrogen from the approaching water molecules around the reductant.

The OSC energy minima of actinyl-EDTA and reductant Fe^{2+} appear at a distance of An-Fe around 5.25-6.75 Å (Fig. 4). The uphill energy slopes start from these distances towards the OSC-ISC activation energy barriers before going down towards the local energy minima of the ISCs. The activation energy barrier for the transition from OSC to ISC results from the relocation of water, which was located in between actinyl-EDTA and reductant, but then, this water has to be squeezed out by the incoming reductant. There are breaking and formation of new bonds between the axial O (O_{ax}) of actinyl or water molecules of the actinyl-EDTA first hydration shell and the water molecules from $Fe_2(OH)_2(H_2O)_{12}$. These rearrangements of bonds cause energy changes to go uphill and downhill, shown as activation energy barriers in the energy curves. When the complexes form ISCs, Fe^{2+} forms a new bond with O_{ax}. Since Fe^{2+} is positively charged, it tends to bond to O_{ax} of actinyl, instead of directly bonding to the actinide ions. Tilting of actinyl-EDTA along the reaction path promotes the formation of Fe^{2+}-O_{ax} bonds.

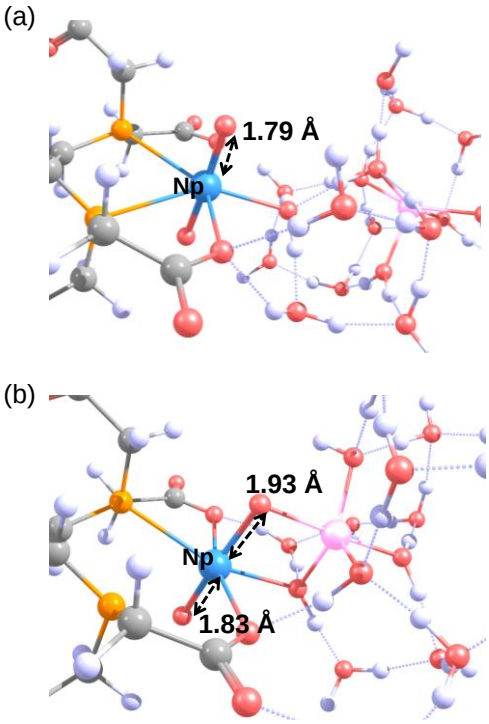

Fig. 5 Geometries of the central portion of outer- and inner-sphere complexes between $[NpO_2(edta)]^{2-}$ and $Fe(OH)_2(H_2O)_{12}$. (a) Outer-sphere complex with Np-Fe distance of 6.0 Å, and (b) inner-sphere complex with Np-Fe distance of 3.0 Å. White-H, gray-C, red-O, orange-N, blue-Np, and pink-Fe. Dotted gray lines represent hydrogen bonds.

The calculated activation energies required to transform OSC to ISC range from 49 to 71 kJ/mol for the different actinyl species (Table 1). They are relatively smaller than those of actinyl tricarbonate complexes ($[AnO_2(CO_3)_3]^{5-/4-}$) determined by Bender *et al*.[4] (however, note that study [4] did not allow for the axial tilt, which may contribute to their activation energies being somewhat higher). Generally, hexavalent actinides have a higher activation energy barrier to transform OSC to ISC compared to the pentavalent actinides, similar to the actinyl tricarbonate complex system.

Experimental[76] and computational[73] values for the U-O_{ax} distances are 1.76 Å for the uranyl aquo complex. However, complexation with ligands in the equatorial plane of the uranyl destabilizes U-O_{ax} bond, so the bond becomes weaker and longer.[77] For this reason, we obtain 1.81 Å U-O_{ax} distance for the uranyl-EDTA complex when uranyl is in the bulk aqueous state. The formation of an inner-sphere complex has little effect on this bond length; the U-O_{ax} bond length becomes 1.82 Å at the energy minimum of the ISC.

In contrast, the An-O_{ax} distance changes for Np^{6+} and Pu^{6+} case. For $[NpO_2(edta)]^{2-}$, the Np-O_{ax} distance is 1.79 Å in the bulk solution, which is ~0.3 Å longer than the aquo-complex Np-O_{ax} distance (Fig. 5). This distance becomes 1.83 Å when it forms an

ISC accompanied by electron transfer (at Np-Fe distance = 3 Å). $[PuO_2(edta)]^{2-}$ also shows an increased Pu-O_{ax} distance when it forms an OSC accompanied by an electron transfer (from 1.78 Å to 1.83 Å). The increased An-O_{ax} distance (~0.05 Å) could be evidence of the reduction of Np and Pu from a hexavalent to a pentavalent species, and will be discussed in more detail in Section 3.5. In addition, when O_{ax} is directly bonded to Fe^{2+} at a very close distance between An-Fe in the inner-sphere complex stage, it shows even longer An-O_{ax} distances (1.93 Å for Np^{6+}, 1.92 Å for Pu^{6+}) due to the strong interaction with Fe^{2+}; at that point, it is both an axial actinyl O atom as well as a bridging one bonded to Fe.

3.5. Charge and spin population analysis

In order to quantify the actual electron transfer between the two reactants, population analysis was used to calculate the charge and spin of individual atoms. Gaussian09 uses the Mulliken population analysis method as a default. Mulliken population analysis[78, 79] is a computationally straightforward and longstanding method, so it is easy to be incorporated in many software packages and most widely used. The drawback of this method is that it depends strongly on the basis sets used and is not reliable for large atomic bases. In contrast, the Bader method (Atoms In Molecules method)[80] uses topological properties of the electron density, with each Bader volume boundary about a given atom defined as where the Laplacian (second derivative) of the electron density equals zero. After this ionic volume has been determined, charge and spin density can then be integrated over this volume to obtain the charge and spin of each individual atom. Even though this method can be computationally expensive, it is less dependent on basis sets and is more reliable with larger basis sets.[81, 82] In this study, the Bader method is used to estimate charge and spin populations. Population analysis using the Bader method shows the evidence of the reduction of actinyls with hexavalent actinides by Fe^{2+} as a reductant. For the reaction of $[NpO_2(edta)]^{2-}$ with the Fe^{2+} (Fig. 6b), the system energy has two deep energy wells at distances where the reactants form ISC (ISC 1 at Np-Fe distance = 3.75 Å) and electron transfer occurs (ISC 2 at Np-Fe distance = 3 Å). Bader charge and spin populations for both Np and Fe show significant and well-defined changes at the ISC 2 energy minimum. The Np spin changes from -1 to -2, which means a reduction from Np^{6+} to Np^{5+} with an opposite spin direction to Fe (anti-ferromagnetic configuration). The Fe spin increases accordingly due to oxidation, indicating a change from ferrous ($4\uparrow$) to ferric iron ($5\uparrow$). Thus, when the aqueous ferrous iron complex approaches the hexavalent neptunyl one, the total spin and charge densities are preserved; in other words, the reaction preserves the angular momentum of the spin, which makes such a reaction kinetically more favorable than a spin-forbidden one. Atomic charges are not as sensitive to oxidation state changes as spin change (*i.e.*, it does typically not change in full integer increments), but they still change when electron transfer occurs.

For the reaction of $[PuO_2(edta)]^{2-}$ with Fe^{2+} (Fig. 6c), electron transfer occurs at the OSC energy minimum, where the spin of

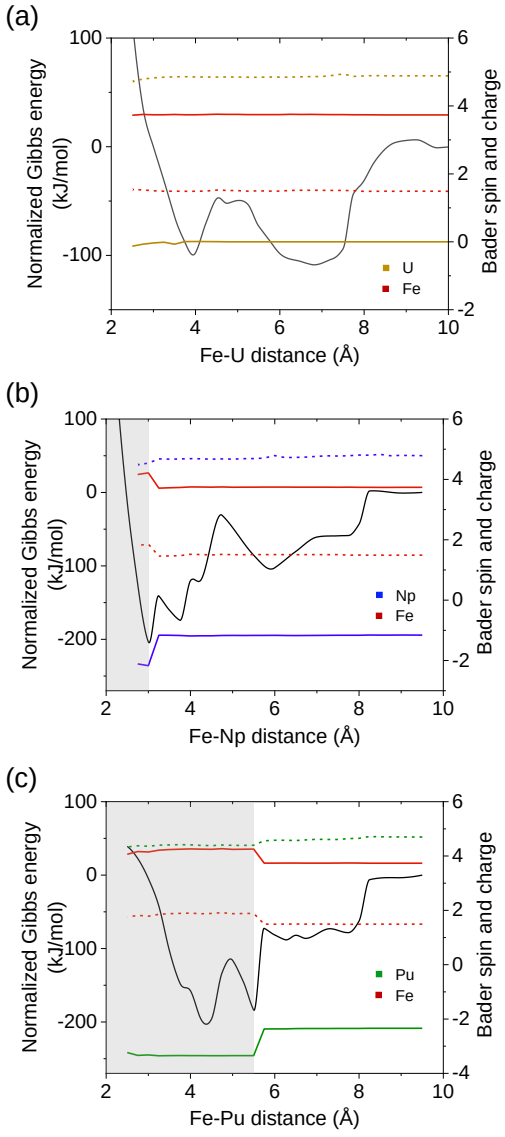

Fig. 6 Bader charge and spin population of An and Fe as a function of An-Fe distance for the reaction of $[AnO_2(edta)]^{2-}$ with a reductant, Fe^{2+}: (a) An=U, (b) An=Np, and (c) An=Pu. Normalized system energy (black line, SOC considered) shows where the spin and charge population change occurs. The shaded area shows where the $[AnO_2(edta)]^{2-}$ complex is reduced by the reductant. No spontaneous electron transfer was observed for U. For Np, it occurs at the inner-sphere complex minimum, and for Pu, at the outer-sphere complex minimum. Golden line – U, blue line – Np, green line – Pu, and red line – Fe. Spin populations are in solid lines, and charge densities are in dotted lines.

Pu^{6+} changes by one (from -2 to -3) to become Pu^{5+} and the spin of Fe^{2+} increases accordingly. The system energy significantly decreases to about -184 kJ/mol when electron transfer occurs, and before that, there is a small energy bump of about 15.7 kJ/mol. This energy bump is required to transfer an electron from Fe^{2+} to Pu^{6+}. Similarly, $[NpO_2(edta)]^{2-}$ has an energy barrier of 33 kJ/mol from ISC 1 to ISC 2. Therefore, one-electron reductions of $[PuO_2(edta)]^{2-}$ and $[NpO_2(edta)]^{2-}$ happen with a relatively low activation energy barrier. The normalized system energies at the inner-sphere complexes energy minima with reduced actinyls are about -203.5 kJ/mol for Np^{6+}

and -196.3 kJ/mol for Pu^{6+} with SOC. Both cases show very stable reduced pentavalent complexes, relative to the corresponding hexavalent ones, after reduction. In contrast, no spontaneous electron transfer is observed for $[UO_2(edta)]^{2-}$ along its reaction path (Fig. 6a). For Np and Pu, which showed reduction of actinides during the reaction paths, spin density changes and potential spin contamination are discussed in Table S3 of the Supplementary Information.

3.6. Formation of An(IV)-EDTA complex

For the potential reduction of pentavalent actinide ions in $[AnO_2(edta)]^{3-}$ by Fe^{2+} from solution, with the corresponding energy curves shown in Figs. 4(b), (d), and (f), the population analysis for all three reaction pairs (U, Np, Pu with Fe) does not indicate any spontaneous electron transfer, despite all of them form stable ISCs with the reductant. The most likely explanation for this is that for An^{5+} in AnO_2^+ getting reduced to An^{4+}, significant geometry rearrangements are required. Because U^{4+} has a coordination number of 8-9,[83] *e.g.*, with a tetrahedral environment of four OH^- and completing a distorted cube with a complementary tetrahedral environment of four additional H_2O molecules or ligands from EDTA, thus abandoning the linear geometry with O atoms. This makes it hard to transfer an electron to reduce U^{5+} to U^{4+} in our calculation setup that tends to preserve the linear actinyl structure. Nonetheless, we manually rearranged the ISC geometry of $[AnO_2(edta)]^{3-}$ with Fe^{2+} as a reductant to make An(IV)-EDTA complexes in order to see the thermodynamic favorability of the reduction from An(V)-EDTA to An(IV)-EDTA. From the optimized ISC geometry of $[AnO_2(edta)]^{3-}$, we first turned the uranyl O_{ax} atoms into hydroxide ligands in an approximate tetrahedral environment. We then added two more OH^- ligands by rearranging water molecules from the hydration sphere. The total number of atoms was kept the same for the two systems.

Several geometries were tested with the charge and spin configuration of U^{4+} and Fe^{3+}, and the geometry shown in Fig. 7 was found to be the most stable for this system. U^{4+} ended up with eight-fold coordination with six O and two N. U-O distances are 2.33-2.42 Å for five O, even the ones in carboxylic groups of EDTA, and 2.19 Å with a free OH^- (this distance is comparable to the calculated U-O distance in $U(OH)_4$). U-N distances are ~2.8 Å. Compared to the U-O distances in uraninite (~2.368 Å), four of the coordinated O in our calculated U^{4+} geometry have shorter distances while the other two O and the two N show longer distances than U-O in uraninite. The reason for those longer distances than in the uraninite environment is probably due to the steric strains of the EDTA. Moreover, the system energy of the configuration shown in Fig. 7 is higher than that of the ISC energy minimum of $[UO_2(edta)]^{3-}$ (by 22.5 kJ/mol) with the same number of atoms of each type, which means greater stability of EDTA complexing UO_2^+ than U^{4+}. Thus, it is thermodynamically uphill to transfer an electron from Fe^{2+} to U^{5+} unless spin-orbit coupling is considered; if it is, the reaction becomes slightly favorable (-6.5 kJ/mol).

In the case of Pu^{4+}, the system becomes more stable (ΔG = -50.2kJ/mol without SOC, and -59.0 kJ/mol with SOC) than that of PuO_2^+. Thus, the reduction of PuO_2^+-EDTA is highly favorable, which agrees well with the previous experiments.[22, 23] The Pu(IV)-EDTA complex structure was constructed in the same manner as U^{4+}, and the final optimized geometry shows the same coordination as U^{4+}. Pu-O distances are 2.32-2.33 Å, except the one with free OH^- (2.20 Å). Pu-N distances are shorter than the U^{4+} result, which are 2.72 Å and 2.76 Å (Fig. 7b).

For Np^{4+}, the system energy was slightly more stable than that of NpO_2^+ (-5.1 kJ/mol without SOC, and -18.5 kJ/mol with SOC). Since there is little difference in the system energy between Np^{4+} and Np^{5+}, unless there is enough energy input to overcome the activation energy barrier for atomic rearrangement and proton transfer, the formation of tetravalent Np complexed by EDTA would be slow. This is in agreement with experiments by Reed *et al*.[22] who showed that Np^{5+} is the predominant species in Np-EDTA solution. The kinetic reaction path, however, is not easy to reconstruct, and the related activation energy barrier for the rearrangement of atoms and molecules is difficult to quantify. This is not only because the geometry of the immediate coordination environment of the actinide ion changes, but also significant proton hopping would be involved. This is done "by hand" in this study, but requires proton hopping back and forth between functional groups and adjacent water molecules.

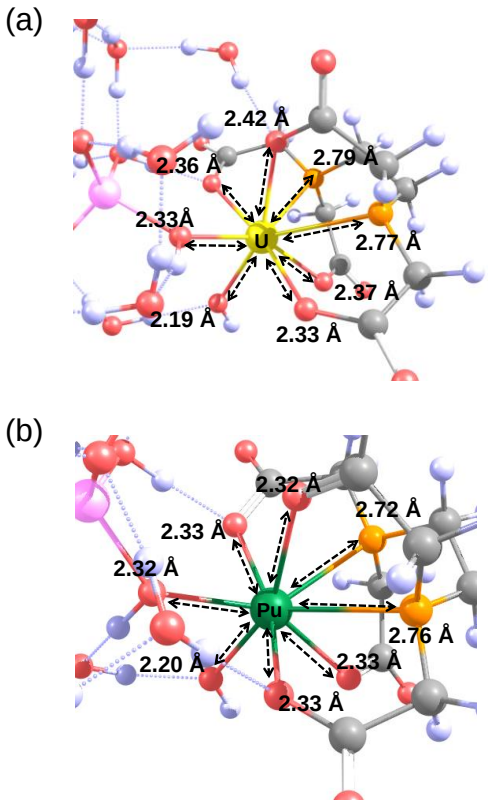

Fig. 7 (a) U^{4+}-EDTA and (b) Pu^{4+}-EDTA complex geometries using the same number of atoms with $[UO_2(edta)]^{3-}$ dnd $[PuO_2(edta)]^{3-}$ system. U and Pu are in eight-fold coordination with EDTA and the water molecules around them. White-H, gray-C, red-O, orange-N, yellow-U, green-Pu, and pink-Fe. The dotted gray lines indicate hydrogen bonds.

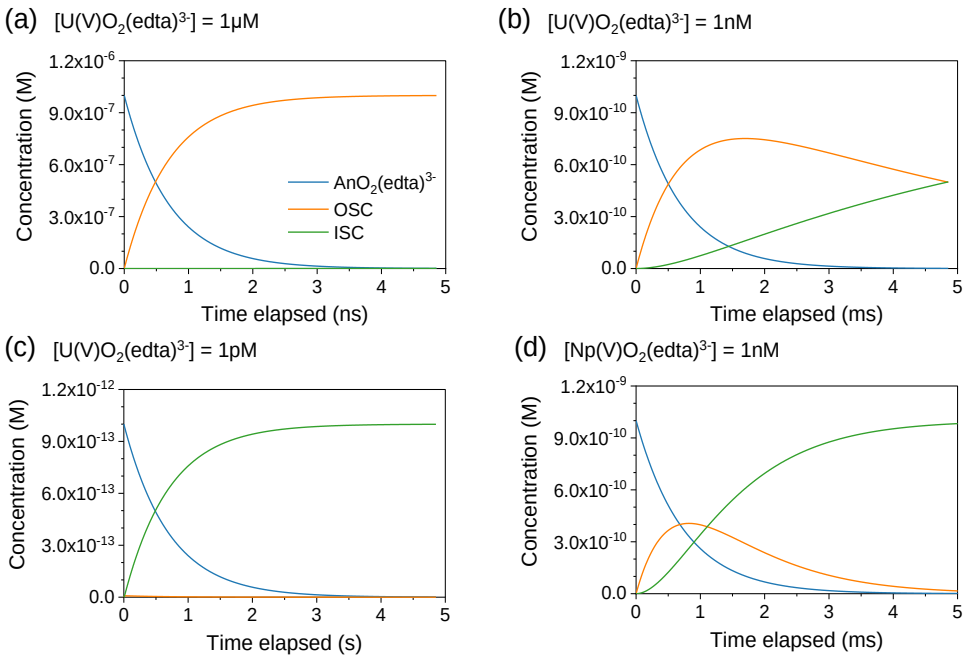

Fig. 8 Concentration changes of $AnO_2(edta)^{3-}$ species over time in the reaction with a reductant Fe^{2+}. (a) $[UO_2(edta)]^{3-}$ = 1 μM, $[Fe^{2+}]$ = 1 mM, (b) $[UO_2(edta)]^{3-}$ = 1 nM, $[Fe^{2+}]$ = 1 μM, and (c) $[UO_2(edta)]^{3-}$ = 1 pM, $[Fe^{2+}]$ = 1 nM, and (d) $[NpO_2(edta)]^{3-}$ = 1 nM, $[Fe^{2+}]$ = 1 μM. $AnO_2(edta)^{3-}$ in bulk solution – blue, OSC – orange, and ISC – green solid line.

3.7. Reaction modeling

A computational code developed by Bender *et al*.[26] was used to see how the concentrations of each species evolve over time. Using the calculated values for R_r, E_a, λ (distance between two energy minima in the energy curve), and the initial reactant concentrations, the program calculates the reaction rate constants, initial collision rates, and half-life time (time at which half the concentration of this species is lost due to reactions) of each complex. The concentration changes of each species over time are calculated using eqns (1) through (3). Because the reaction rate is related to the concentrations of each intermediate complex at a given time, the program calculates the reactant concentrations iteratively for every time step. These time increments have to be chosen to be orders of magnitude smaller than the half time to capture the progression into the different species correctly. The calculated attempt frequencies for all six reaction pairs were in the range of 7.62×10^{11} to 2.07×10^{12} s^{-1}, and the graphs showing the time-resolved development of species concentrations are shown in Fig. 8.

With 1 μM of actinyl-EDTA and 1 mM of reductant, all species showed rapid OSC formations in a few nanoseconds (ns) similar to Fig. 8(a). As shown in Table 1, pentavalent actinide reactions have lower activation energies than those of hexavalent actinides for the transition from OSC to ISC. Thus, the transition from OSC to ISC for pentavalent species is faster than for hexavalent ones. After a few milliseconds (ms), the accumulation of ISC is observed for UO_2^+, NpO_2^+, and PuO_2^+. This is not the case for hexavalent actinides which require a significantly longer time (on the order of a few hundred ms to a few seconds) to be converted to an ISC.

With higher reactant concentrations, the formation of OSC becomes faster because of the increased probability of reactant collision. Similarly, a lower initial reactant concentration decreases the OSC formation rate. Still, rate constants for the transition from OSC to ISC remain the same (the rate constant for this transition does not depend on reactant concentrations, but on the E_a and attempt frequency). Thus, we can see some accumulation of OSC along with the accumulation of ISC over our calculated time scale with 1 nM of $AnO_2(edta)^{3-}$ and 1 μM of reductant (Fig. 8b and d). Since the reaction constant for UO_2^+ is smaller than for NpO_2^+, UO_2^+ takes a longer time to reach 95% of ISC (20 ms) in solution than NpO_2^+ (4 ms) (Table 3). Reactions between 1 pM of $AnO_2(edta)^{3-}$ and 1 nM of reductant take three to four seconds until most of the reactants are converted to ISC configurations due to the very slow collision rate. Table 3 summarizes how long it takes for 50% and 95% of reactants to form ISCs for concentrations of $[AnO_2(edta)]^{2-/3-}$ = 1 nM and $[Fe^{2+}]$ = 1 μM. While dehydration of Np(VI) and Pu(VI)-EDTA complexes is slower than for the respective U(VI) complex, the final electron transfer is faster for the higher actinides.

Table 3 Time spent to 50% and 95% of reactants form ISC in $[AnO_2(edta)]^{2-/3-}$ = 1 nM, $[Fe^{2+}]$ = 1 μM solutions. (Units in ms.)

	50%	95%
UO_2^{2+}	37	159
UO_2^+	4	20
NpO_2^{2+}	2271	9779
NpO_2^+	1.4	4
PuO_2^{2+}	256	1103
PuO_2^+	0.9	2.6

3.8. Actinyl-EDTA reduction at low pH

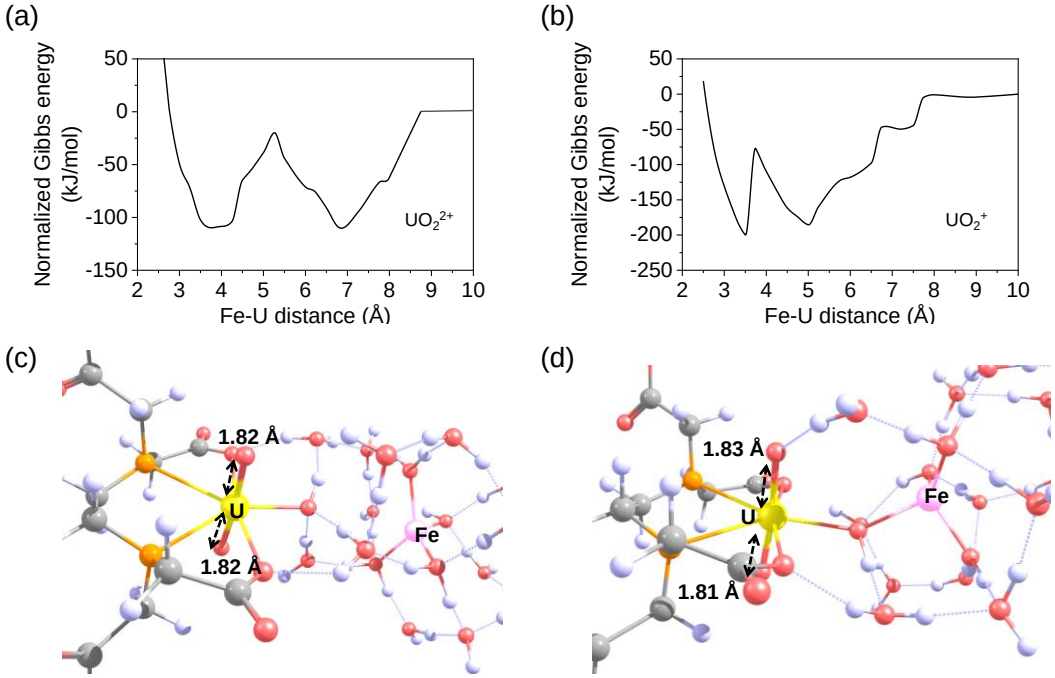

Fig. 9 System energy curve for the reaction of $Fe(OH)_2(H_2O)_{12}^0$ with (a) $[UO_2(Hedta)]^-$ and (b) $[UO_2(Hedta)]^{2-}$ in acidic solution. And optimized geometries of $[UO_2(Hedta)]^-$ reacted with Fe^{2+} reductant in acidic solution at U-Fe distance of (c) 6.0 Å (OSC), and (d) 4.25 Å (ISC). White-H, gray-C, red-O, orange-N, yellow-U, and pink-Fe. The dotted gray lines indicate hydrogen bonds.

The reduction of uranyl-EDTA complex with iron at low pH was calculated to see the pH effect on the reaction process. As discussed in Section 3.1, $[UO_2(Hedta)]^-$ are the most abundant species at pH 3 to 5. The reactive radii of these complexes during the reaction path with aqueous Fe are ~8.72 Å for hexavalent U and ~7.89 Å for pentavalent U, which are similar to those calculated for neutral conditions (Fig. 9a and b). It is likely that changes in the size of uranyl-EDTA complexes due to changes in the protonation of EDTA are marginal. However, the calculated activation energy for the reaction of $[UO_2(Hedta)]^-$ with Fe^{2+} is higher than for the reaction in circumneutral pH conditions. The forward reaction activation energies (E_a from OSC to ISC) are 87.9 kJ/mol for UO_2^{2+} and 108.0 kJ/mol for UO_2^+. $E_{a,back}$ (from ISC to OSC) values are 88.6 kJ/mol for UO_2^{2+} and 122.3 kJ/mol for UO_2^+. Thus, the reaction is expected to be much slower at low pH, where the calculated reaction constants are several orders of magnitude smaller than the ones at circumneutral pH conditions.

The reaction curves of $[UO_2(Hedta)]^-$ that show the evolution of the reactant concentrations over time resulted in longer reaction times for the transition to OSC to ISC compared to the ones at neutral conditions. In neutral conditions, it takes 1.9 s to 95% of the reactants ($[UO_2(edta)]^{2-}$ = 1 pM, $[Fe^{2+}]$ = 1 nM) to become ISC, whereas ~2.3 hr in acidic conditions. The reason for this longer reaction time is higher activation energy from OSC to ISC. Since the formation rate of OSC is related to the reactive radius and the reactant concentrations, both acidic and neutral conditions have similar reaction times; it takes less than 3 seconds to consume >99% of the aqueous species and form OSC. The same was observed for $[UO_2(Hedta)]^{2-}$ because it has an even shorter reactive radius.

The U-Fe distances at the OSC and ISC minima are the same for the two different pH conditions. However, unlike in neutral pH conditions, both UO_2^{2+} and UO_2^+ show more stable system energies for ISC than OSC. Geometries of OSC and ISC for $[UO_2(Hedta)]^-$ are shown in Fig. 9(c) and (d). The U-O_{ax} distance is 1.82 Å when the reactants are in OSC, and little difference is observed when an ISC is formed. Since there was no immediate electron transfer during the reaction path, the U-O_{ax} distance stayed almost the same, like in the $[UO_2(edta)]^{2-}$ system.

4. Discussion

The redox mechanism and kinetics of EDTA-complexed actinyl reduction (An = U, Np, and Pu) by ferrous iron were calculated in this study. Even though not all oxidation states of An-EDTA calculated here are common in the environment (*e.g.*, Np(VI) and Pu(VI) are not), we calculated all six combinations for completeness and to explain the mechanism of experimental phenomena about why and why not certain species easily change their oxidation state to a more energetically favorable one and how dehydration kinetics depends on actinide species and oxidation state. The system-energy curves obtained using quantum-mechanical calculations were used to obtain attempt frequencies and activation energies along the reaction paths. These reaction paths are characterized by major reaction steps, such as the reductant getting close enough for the complex to feel interactions, the formation of an outer- and inner-sphere complex, and finally, the actual electron transfer.

In our series of calculations, spontaneous electron transfer occurs for Np and Pu, but not for U. We tested several sets of step-wise calculations starting from a far distance (10~12 Å) for each pair of reactants. Each trial produces slightly different kinetic parameters due to the random geometries of water that lead to different formations of hydrogen bonds and reactant trajectories. Still, we obtained similar kinetic parameters for each set. Repeated calculations with even more different reaction paths would produce more statistically significant values but at a high computational cost. An additional way, however also highly computationally-expensive, to quantify the influence of random hydrogen bond formation and breaking is distance-controlled quantum-mechanical molecular dynamics.[84-86]

There are two possible ways of enhancing the mobility of actinides in solution by organic ligands; (1) forming a complex increases the solubility, and (2) complexation decreases the reduction rate of actinides. Process (1) reduces the concentration of free actinyl in solution, thereby decreasing the ion activity product for the potential precipitation of UO_2 (uraninite, in case there is reduction) or oxidized precipitates such as uranophane ($[Ca(UO_2)_2(SiO_3OH)_2]\cdot 5(H_2O)$), betafite ($(Ca,U)_2(Ti,Nb,Ta)_2O_6(OH)$), studtite ($[(UO_2)O_2(H_2O)_2]\cdot 2(H_2O)$), metastudtite ($[(UO_2)O_2(H_2O)_2]$), or their Np and Pu equivalents. The idea behind the process (2) is that the complex hinders the electron transfer from a reductant towards the actinyl ion.

In the case of neptunyl and plutonyl, Reed *et al*.[22] observed a rapid reduction of $Np(VI)O_2^{2+}$ to $Np(V)O_2^{+}$ and $Pu(VI)O_2^{2+}$ to $Pu(V)O_2^{+}$ in low ionic-strength media with EDTA. Further reduction to the tetravalent actinide is hardly observed for neptunyl, but for plutonyl in this EDTA solution. Our calculations agree well with this experiment, showing immediate electron transfer (change of Bader spin by ~1) when the reactants ($AnO_2(edta)^{2-}$ and Fe^{2+} with An = Np and Pu) form an OSC or ISC. In the result of Bender et al.,[26] which calculated the reduction of free PuO_2^{2+} (aquo-complexed) in the solution with ferrous iron, a one-electron transfer occurred with an activation energy (OSC → ISC) of 45.7 kJ/mol. This value is lower than our calculated value of ISC formation activation energy for $Pu(VI)O_2(edta)^{2-}$ with Fe^{2+}. The attempt frequency (*A*) of aquo-complexed plutonyl is three times bigger than that of EDTA-complexed one, and the resulting rate constant calculated using *A* and E_a is four orders of magnitude higher for the aquo-complexed plutonyl. Thus, complexation with EDTA is not prohibiting but significantly slowing down the reduction of $Pu(VI)O_2(edta)^{2-}$ in solution with ferrous iron. EDTA does not entirely shut down reduction because it is not completely 'wrapping up' the uranyl ion but rather leaves one side open for reductive attack be ferrous iron.

Four out of five trials of the $PuO_2(edta)^{2-}$ reaction series, and two out of four trials of the $NpO_2(edta)^{2-}$ series showed electron transfer with relatively small energy barriers (< 35 kJ/mol). This indicates that electron transfer is not the rate-controlling step for these two species. We also calculated the thermodynamic stability of the Pu(IV) complex, which showed lower system energy than that of Pu(V) explaining the experimental phenomena of Pu^{4+}-EDTA formation in Reed *et al*.[22] However, Pu^{4+}-EDTA is a stable and soluble complex; thus, even if a Pu-EDTA complex is reduced, it still enhances Pu migration in the subsurface and groundwater.[58] $Np(V)O_2(edta)^{3-}$, which is the dominant species of Np in EDTA solution, is also highly soluble,[65] thus promoting Np migration.

It is well known that EDTA enhances the mobility of uranyl by forming soluble and stable complexes.[16, 87, 88] In addition, a reduced reduction rate can further uranyl transport in aqueous environments. Although many previous studies have determined the formation constants of U-EDTA,[68, 89, 90] there is a lack of redox kinetics data. Our calculated result of 60.5 kJ/mol of activation energy for the ISC formation of $U(VI)O_2(edta)^{2-}$ by aqueous ferrous iron is lower than that of $NpO_2(edta)^{2-}$ or $PuO_2(edta)^{2-}$ (Table 1). Even though most of the U-EDTA with a significantly higher concentration of Fe^{2+} forms ISC in a second, immediate electron transfer was not observed for the uranyl-EDTA, but for Np- and Pu-EDTA. In this study, we calculated how easily ISC can be formed but not really about electron transfer. We would have to quantify the kinetics of electron transfer, such as using Marcus theory, which is beyond the scope of this study.

Often in nature, microbes facilitate the reduction of free-uranyl and uranyl-EDTA.[16, 17, 87] Suzuki *et al*. observed the dissolved U fraction after 21 hours of incubation with microbes (*Shewanella putrefaciens*) decreased to about 9% due to the significant reduction of U(VI) to U(IV).[16] Sheng *et al*. obtained no measurable U(VI) reduction without microbes in solution, but observed U(IV) precipitates with *Shewanella oneidensis* MR-1.[17] Adding EDTA to this solution decreased reductive precipitation significantly; however, more reduction occurred at higher EDTA concentrations. Their proposed mechanism is that EDTA facilitates U reduction by removing U^{4+} in the form of U^{4+}-EDTA from the cell surface, so the reduction site of the bacterial cell can be free for further reduction.

The photocatalytic reduction can also facilitate the reduction of uranyl-EDTA.[19-21] Under UV light, Chen *et al*. observed the reduction of U(VI) on the catalyst surface, such as TiO_2 or Pt/TiO_2, with EDTA serving as the electron donor.[19] Kim *et al*. reported the effect of organic ligands (oxalate, acetate, hydroquinone, and EDTA) in the photochemical reduction of uranyl. With these organic ligands as electron donors, U(VI) (as uranyl) reduction to U(V) and U(IV) was observed, particularly in combination with UV light and a TiO_2 photocatalyst.[20] Proton-coupled electron transfer helps reduce U as well, as shown in some prior works for plutonyl aquo-complexes[26] and uranyl-tricarbonate ones [4, 6].

However, both UO_2^{2+}-EDTA and U^{4+}-EDTA are soluble,[16, 87, 91] so regardless of the U oxidation state, EDTA complexation can enhance the migration of U to some degree. Thus, in terms of environmental remediation, EDTA can be of concern because it forms a stable and soluble complex with actinyls and enhances their mobility. In terms of a decontamination-cleaning agent, EDTA is efficient due to its ability to form strong soluble complexes and to reduce Np and Pu rapidly. However, EDTA in the mixed secondary waste is problematic after its use, because removal of EDTA is not easy and EDTA complexes are not readily

degradable by conventional biological treatment processes.[13, 92, 93]

Calculations of $[UO_2(Hedta)]^{-/2-}$ reduction give clues on how uranyl-EDTA reduction kinetics would change in lower pH ranges (*i.e.*, acidic condition). The calculated reaction rate constant from OSC to ISC is ~10^4 times higher in neutral conditions. This agrees well with the experimental observation by Wang *et al*.[15] that neutral pH conditions result in faster reduction rates than acidic ones. They obtained the maximum apparent reaction rate constant at pH 7.4, and it was close to zero at pH lower than 4. Since the effect of pH conditions is considerable, it could possibly be used to control the reduction rates in radioactive waste treatment or other industrial settings. The geometries of uranyl-EDTA are not well defined yet, so we suggested a tetra-dentate geometry of $[UO_2(Hedta)]^-$ as shown in Fig. 2(b) based on our DFT calculation result. When we compare the pK_a values of the carboxyl group and amino group, it is expected that the amino groups get protonated before the carboxyl groups with decreasing pH. However, our calculations on the uranyl-EDTA complex show proton transfer from N to $O_{carboxyl}$ such that the uranyl can stay five-coordinated in the equatorial plane, and the resulting geometry with protonated carboxyl has lower system energy. We made the same observation of carboxyl protonation for calculations on $Ca(edta)^{2-}$. DFT calculations started from a stable 6-coordinated Ca structure, a proton initially attached to an amine N of EDTA was observed moving to one of the carboxyl groups by proton transfer through the nearby water chains. The resulting $Ca(Hedta)^-$ structure (with a protonated carboxylate) was energetically more stable than the starting geometry (with a protonated N). It is likely the protonation of N obstructs the 6-coordinated stabilized Ca geometry, thus becoming less favorable. The $Fe(II)Hedta(H_2O)^-$ structure reported by Mizuta *et al*.[94] using single crystal XRD analysis also has a protonated carboxylate, not an amino group. The same was observed for Mn(II) and Cd(II) complexes.[95, 96]

By using the parameters in Table 2, we generated time evolution graphs of the reactant concentrations. From these graphs, we were able to estimate the time scales of the reactions (An(VI/V)-EDTA with Fe^{2+}) in different initial concentrations and predict which stage (bulk, OSC, or ISC) is dominant and how it changes over time. Calculated $t_{1/2}$ from bulk solution species to OSC is a few hundred ms, and it will take a few seconds to transform all the aqueous species into OSC, using concentrations of 1 pM of $[AnO_2(edta)]^{2-/3-}$ and 1 nM of Fe^{2+}. This time scale decreases even more, if reactant concentrations are higher due to the higher possibility of collision between the two reactants. Thus, by adjusting the initial concentration, the overall reaction time scale can be sufficiently long and measurable experimentally. Still, solution pH, surface adsorption, and microbial activities might change the reaction rates in natural environments.

5. Conclusions

The calculations in this study present detailed reaction kinetics data for the reduction of actinyl-EDTA complexes by Fe^{2+}. EDTA is a widespread chemical used in industry and agriculture, therefore it is important to understand its effect on the fate of potential contaminants in both thermodynamic and kinetic perspectives. Our results show that EDTA complexation does not prohibit the reduction of neptunyl-EDTA and plutonyl-EDTA in the presence of ferrous iron, with relatively low ISC formation activation energies and immediate electron transfer after the formation of OSC or ISC. We find that the electron is transferred mainly from iron and it is not EDTA that functions as the major electron donor. For these reactions, electron transfer is not found to be the rate-limiting step. Since the formation of OSC from aqueous species by collisions of reactants is relatively fast compared to other sub-steps (OSC to ISC, and electron transfer), it appears that OSC to ISC transition is the rate-limiting step for these reactions.

In contrast to Np and Pu, no immediate electron transfer was observed for uranyl-EDTA calculation. However, the activation energy for the ISC formation is lower than Np and Pu (< 60.5 kJ/mol), and a lower activation energy increases the likelihood of electron transfer. Thus, there is more to be explored for uranyl-EDTA, such as the effect of UV light-induced or mineral surface- and microbe-catalyzed electron transfer, in addition to our calculation result. When in acidic conditions, the energy barrier for the ISC formation increases, meaning the reaction becomes much slower. And at this low pH conditions, microbial reduction would be mostly prohibited, making the reduction even harder.

This series of calculations was performed for a homogeneous solution, but mineral surfaces can facilitate the redox reaction of actinyls in nature; the same would be true for other catalytic reactions, for example, in separation operations. It is well known that hematite, goethite,[97] magnetite,[98] and also sulfides, such as pyrite,[99-101] provide surfaces for uranium adsorption and catalyze the reduction of U by Fe^{2+}. The addition of mineral surfaces to our approach could be performed in the future. Also, modeling the microbial activity by adding enzymes with other organic electron sources (*e.g.*, citrate or hydroquinone) can be performed using computational approaches. Our method can also readily be applied to other organic ligands, such as citric acid, oxalic acid, or NTA (nitrilotriacetic acid),[8, 16, 87] to better understand their effect on actinyl transport in the environment.

Author contributions

Sooyeon Kim: conceptualization, formal analysis, investigation, visualization, writing - original draft. Will M. Bender: methodology, software, writing - reviewing & editing. Udo Becker: conceptualization, methodology, software, funding acquisition, project administration, supervision, writing - reviewing & editing.

Conflicts of interest

There are no conflicts to declare.

Acknowledgments

This research was supported by funding from the U.S. Department of Energy's (DOE) Office of Science, Office of Basic Energy Sciences (BES), Chemical Sciences, Geosciences, & Biosciences (CSGB) Division for the topics of Heavy Element Chemistry and Geoscience (grant number DE-FG02-06ER15783, Funder Id: http://dx.doi.org/10.13039/100006151). Part of the calculations for this study were carried on the Flux high-performance computing cluster managed by University of Michigan Advanced Research Computing Technology Services (ARC-TS).

References

1. National Research Council, in *Uranium mining in virginia: Scientific, technical, environmental, human health and safety, and regulatory aspects of uranium mining and processing in Virginia*, Washington (DC), 2011, DOI: 10.17226/13266.
2. A. Bleise, P. R. Danesi and W. Burkart, *J Environ Radioact*, 2003, **64**, 93-112.
3. D. Langmuir, *Aqueous environmental geochemistry*, Prentice Hall, Upper Saddle River, New Jersey, 1997.
4. W. M. Bender and U. Becker, *Radiochim Acta*, 2019, **108**, 165-184.
5. D. E. Morris, *Inorg Chem*, 2002, **41**, 3542-3547.
6. M. C. F. Wander, S. Kerisit, K. M. Rosso and M. A. A. Schoonen, *J Phys Chem A*, 2006, **110**, 9691-9701.
7. Y. Suzuki, T. Nankawa, T. Ozaki, T. Ohnuki, A. J. Francis, Y. Enokida and I. Yamamoto, *J Nucl Sci Technol*, 2007, **44**, 1227-1232.
8. R. Ganesh, K. G. Robinson, G. D. Reed and G. S. Sayler, *Appl Environ Microb*, 1997, **63**, 4385-4391.
9. Y. Suzuki, T. Nankawa, T. Yoshida, T. Ozaki, T. Ohnuki, A. J. Francis, S. Tsushima, Y. Enokida and I. Yamamoto, *Radiochim Acta*, 2006, **94**, 579-583.
10. J. Wan, T. K. Tokunaga, E. Brodie, Z. Wang, Z. Zheng, D. Herman, T. C. Hazen, M. K. Firestone and S. R. Sutton, *Environ Sci Technol*, 2005, **39**, 6162-6169.
11. S. Doudou, K. Arumugam, D. J. Vaughan, F. R. Livens and N. A. Burton, *Phys Chem Chem Phys*, 2011, **13**, 11402-11411.
12. L. Chen, D. B. Chamberlain, C. Conner and G. F. Vandegrift, *A survey of decontamination processes applicable to DOE nuclear facilities*, United States, 1997.
13. C. Oviedo and J. Rodríguez, *Quim Nova*, 2003, **26**, 901-905.
14. A. S. Allard, L. Renberg and A. H. Neilson, *Chemosphere*, 1996, **33**, 577-583.
15. Z. Wang, K. B. Wagnon, C. C. Ainsworth, C. Liu, K. M. Rosso and J. K. Fredrickson, *Radiochim Acta*, 2008, **96**, 599-605.
16. Y. Suzuki, K. Tanaka, N. Kozai and T. Ohnuki, *Geomicrobiol J*, 2010, **27**, 245-250.
17. L. Sheng, J. Szymanowski and J. B. Fein, *Geochim Cosmochim Ac*, 2011, **75**, 3558-3567.
18. D. R. Lovley, E. J. P. Phillips, Y. A. Gorby and E. R. Landa, *Nature*, 1991, **350**, 413-416.
19. J. Chen, D. F. Ollis, W. H. Rulkens and H. Bruning, *Colloid Surface A*, 1999, **151**, 339-349.
20. Y. Kim, M. C. Marcano, B. R. Ellis and U. Becker, *Am J Sci*, 2018, **318**, 949-968.
21. C. Cerrillos and D. F. Ollis, *Journal of Advanced Oxidation Technologies*, 1998, **3**, 167-173.
22. D. T. Reed, D. G. Wygmans, S. B. Aase and J. E. Banaszak, *Radiochim Acta*, 1998, **82**, 109-114.
23. I. AlMahamid, K. A. Becraft, N. L. Hakem, R. C. Gatti and H. Nitsche, *Radiochim Acta*, 1996, **74**, 129-134.
24. H. Boukhalfa, S. D. Reilly, W. H. Smith and M. P. Neu, *Inorg Chem*, 2004, **43**, 5816-5823.
25. P. Cauchetier and C. Guichard, *Radiochim Acta*, 1973, **19**, pp. 137-146. .
26. W. M. Bender and U. Becker, *Am J Sci*, 2018, **318**, 893-920.
27. P. Zarzycki, S. Kerisit and K. M. Rosso, *J Phys Chem C*, 2015, **119**, 3111-3123.
28. S. D. Taylor, M. C. Marcano, K. M. Rosso and U. Becker, *Geochim Cosmochim Ac*, 2015, **156**, 154-172.
29. D. Renock and U. Becker, *Geochim Cosmochim Ac*, 2010, **74**, 4266-4284.
30. A. D. Becke, *J Chem Phys*, 1993, **98**, 5648-5652.
31. C. T. Lee, W. T. Yang and R. G. Parr, *Phys Rev B*, 1988, **37**, 785-789.
32. G. A. Shamov and G. Schreckenbach, *J Phys Chem A*, 2005, **109**, 10961-10974.
33. P. Wahlin, C. Danilo, V. Vallet, F. Real, J. P. Flament and U. Wahlgren, *J Chem Theory Comput*, 2008, **4**, 569-577.
34. K. Arumugam and N. A. Burton, *Physical Chemistry Chemical Physics*, 2019, **21**, 3227-3241.
35. P. Di Bernardo, P. L. Zanonato, F. Benetollo, A. Melchior, M. Tolazzi and L. Rao, *Inorg Chem*, 2012, **51**, 9045-9055.
36. A. Fouqueau, S. Mer, M. E. Casida, L. M. Lawson Daku, A. Hauser, T. Mineva and F. Neese, *J Chem Phys*, 2004, **120**, 9473-9486.
37. C. Adamo and V. Barone, *J Chem Phys*, 1999, **110**, 6158-6170.
38. Y. Zhao and D. G. Truhlar, *J Chem Phys*, 2006, **125**.
39. W. Küchle, M. Dolg, H. Stoll and H. Preuss, *J Chem Phys*, 1994, **100**, 7535-7542.
40. M. Dolg, U. Wedig, H. Stoll and H. Preuss, *J Chem Phys*, 1987, **86**, 866-872.
41. W. Küchle, M. Dolg, H. Stoll and H. Preuss, *Mol Phys*, 1991, **74**, 1245-1263.
42. T. H. Dunning, *J Chem Phys*, 1989, **90**, 1007-1023.
43. H. F. Schaefer, *Methods of electronic structure theory*, Plenum Press, New York, 1st edn., 1977.
44. G. Schreckenbach and G. A. Shamov, *Accounts of Chemical Research*, 2010, **43**, 19-29.
45. E. R. Batista, R. L. Martin, P. J. Hay, J. E. Peralta and G. E. Scuseria, *J Chem Phys*, 2004, **121**, 2144-2150.
46. M. J. Apted, G. A. Waychunas and G. E. Brown, *Geochim Cosmochim Ac*, 1985, **49**, 2081-2089.
47. A. A. Jarzecki, A. D. Anbar and T. G. Spiro, *J Phys Chem A*, 2004, **108**, 2726-2732.
48. L. Dégrève and C. Quintale, *J Electroanal Chem*, 1996, **409**, 25-31.
49. H. Ohtaki and T. Radnai, *Chem Rev*, 1993, **93**, 1157-1204.
50. T. Remsungnen and B. M. Rode, *Chem Phys Lett*, 2004, **385**, 491-497.
51. L. Guimarães, H. A. de Abreu and H. A. Duarte, *Chem Phys*, 2007, **333**, 10-17.
52. F. A. Cotton, L. M. Daniels, C. A. Murillo and J. F. Quesada, *Inorg Chem*, 1993, **32**, 4861-4867.
53. G. J. Herdman and G. W. Neilson, *J Phys-Condens Mat*, 1992, **4**, 649-653.

54. M. Cossi, N. Rega, G. Scalmani and V. Barone, *J Comput Chem*, 2003, **24**, 669-681.
55. D. F. Shriver, M. T. Weller, T. Overton, J. Rourke and F. A. Armstrong, *Inorganic chemistry*, W.H. Freeman and Company, New York, 6th edn., 2014.
56. Y. Tachi, T. Nakazawa, M. Ochs, K. Yotsuji, T. Suyama, Y. Seida, N. Yamada and M. Yui, *Radiochim Acta*, 2010, **98**, 711-718.
57. K. Furukawa, Y. Takahashi and H. Sato, *Geochim Cosmochim Ac*, 2007, **71**, 4416-4424.
58. N. L. Hakem, P. G. Allen and E. R. Sylwester, *J Radioanal Nucl Ch*, 2001, **250**, 47-53.
59. D. R. Lide and H. V. Kehiaian, *CRC handbook of thermophysical and thermochemical data*, CRC Press, Boca Raton, New York, 1994.
60. M. M. Askarieh, M. I. Hansford, S. Staunton and L. V. C. Rees, *Complexation of Np(V) in aqueous solutions*, Commission of the European Communities, Luxembourg, 1993.
61. K. A. Kraus, F. Nelson and G. L. Johnson, *J Am Chem Soc*, 1949, **71**, 2510-2517.
62. M. E. Glicksman, *Diffusion in solids : field theory, solid-state principles, and applications*, Wiley, New York, 2000.
63. M. Reich, S. Utsunomiya, S. E. Kesler, L. M. Wang, R. C. Ewing and U. Becker, *Geology*, 2006, **34**, 1033-1036.
64. M. Reich, R. C. Ewing, T. A. Ehlers and U. Becker, *Geochim Cosmochim Ac*, 2007, **71**, 3119-3130.
65. W. Hummel, F. J. Mompean, M. Illemassène and J. Perrone, *Chemical thermodynamics of compounds and complexes of U, Np, Pu, Am, Tc, Se, Ni, and Zr, with selected organic ligands*, Elsevier Science, Amsterdam, Boston, 2005.
66. K. Nakamoto, Y. Morimoto and A. E. Martell, *J Am Chem Soc*, 1963, **85**, 309-313.
67. D. Harvey, *Modern analytical chemistry*, McGraw-Hill, Kingsport, Tennessee, 1st edn., 2000.
68. M. Brighli, J. Lagrange and P. Lagrange, *Polyhedron*, 1984, **3**, 469-474.
69. X. Li, Z. Zhang, L. R. Martin, S. Luo and L. Rao, *Rsc Adv*, 2016, **6**, 114916-114926.
70. M. Gavrilescu, L. V. Pavel and I. Cretescu, *J Hazard Mater*, 2009, **163**, 475-510.
71. D. Hagberg, G. Karlstrom, B. O. Roos and L. Gagliardi, *J Am Chem Soc*, 2005, **127**, 14250-14256.
72. M. Duvail, T. Dumas, A. Paquet, A. Coste, L. Berthon and P. Guilbaud, *Phys Chem Chem Phys*, 2019, **21**, 7894-7906.
73. P. J. Hay, R. L. Martin and G. Schreckenbach, *J Phys Chem A*, 2000, **104**, 6259-6270.
74. V. Vallet, L. Maron, B. Schimmelpfennig, T. Leininger, C. Teichteil, O. Gropen, I. Grenthe and U. Wahlgren, *J Phys Chem A*, 1999, **103**, 9285-9289.
75. S. Tsushima, U. Wahlgren and I. Grenthe, *J Phys Chem A*, 2006, **110**, 9175-9182.
76. P. G. Allen, J. J. Bucher, D. K. Shuh, N. M. Edelstein and T. Reich, *Inorg Chem*, 1997, **36**, 4676-4683.
77. V. Vallet, U. Wahlgren and I. Grenthe, *J Phys Chem A*, 2012, **116**, 12373-12380.
78. R. S. Mulliken, *J Chem Phys*, 1955, **23**, 1833-1840.
79. R. S. Mulliken, *J Chem Phys*, 1955, **23**, 1841-1846.
80. R. F. W. Bader, *Atoms in molecules: A quantum theory*, Oxford University Press, Oxford, New York, 1990.
81. D. C. Young, *Computational chemistry: A practical guide for applying techniques to real world problems*, Wiley, New York, 2001.
82. V. Brázdová and D. R. Bowler, *Atomistic computer simulations: A practical guide*, Wiley-VCH Verlag GmbH & Co. KgaA, Weinheim, 2013.
83. C. Hennig, S. Tsushima, V. Brendler, A. Ikeda, A. C. Scheinost and G. Bernhard, *Coordination of U(IV) and U(VI) sulfate hydrate in aqueous solution. In: B.J. Merkel, A. Hasche-Berger, Uranium, mining and hydrogeology.*, Springer, Berlin Heidelberg, Berlin, Heidelberg, 2008.
84. Y. Ming, N. Kumar and D. J. Siegel, *ACS Omega*, 2017, **2**, 4921-4928.
85. C. Boehme and D. Marx, *J Am Chem Soc*, 2003, **125**, 13362-13363.
86. A. Motta, M. P. Gaigeot and D. Costa, *J Phys Chem C*, 2012, **116**, 23418-23427.
87. J. R. Haas and A. Northup, *Geochemical Transactions*, 2004, **5**, 41-48.
88. W. Luo and B. Gu, *Environ Sci Technol*, 2011, **45**, 2994-2999.
89. R. M. Smith and A. E. Martell, *Sci Total Environ*, 1987, **64**, 125-147.
90. T. R. Bhat and M. Krishnamurthy, *Journal of Inorganic and Nuclear Chemistry*, 1964, **26**, 587-594.
91. W. Hummel, I. Puigdomenech, L. F. Rao and O. Tochiyama, *Cr Chim*, 2007, **10**, 948-958.
92. A. F. Gaudy and E. T. Gaudy, *Microbiology for environmental scientists and engineers*, McGraw-Hill, New York, 1980.
93. C. P. Huang, M. C. Hsu and P. Miller, *J Environ Eng-Asce*, 2000, **126**, 919-924.
94. T. Mizuta, J. Wang and K. Miyoshi, *Inorg Chim Acta*, 1995, **230**, 119-125.
95. J. C. Belmont-Sánchez, N. Ruiz-González, A. Frontera, A. Matilla-Hernández, A. Castiñeiras and J. Niclós-Gutiérrez, *Crystals*, 2020, **10**.
96. I. N. Polyakova, A. L. Poznyak, V. S. Sergienko and L. V. Stopolyanskaya, *Crystallogr Rep+*, 2001, **46**, 40-45.
97. C. K. D. Hsi and D. Langmuir, *Geochim. Cosmochim. Acta*, 1985, **49**, 1931-1941.
98. N. H. Sagert, C. H. Ho and N. H. Miller, *J Colloid Interf Sci*, 1989, **130**, 283-287.
99. K. Arumugam, D. Renock and U. Becker, *Phys Chem Chem Phys*, 2019, **21**, 6415-6431.
100. D. Renock, M. Mueller, K. Yuan, R. C. Ewing and U. Becker, *Geochim Cosmochim Ac*, 2013, **118**, 56-71.
101. K. Yuan, D. Renock, R. C. Ewing and U. Becker, *Geochim Cosmochim Ac*, 2015, **156**.